iScience

CellPress

Article

# Mediation of Electron Transfer by Quadrupolar Interactions: The Constitutional, Electronic, and Energetic Complementarities in Supramolecular Chemistry

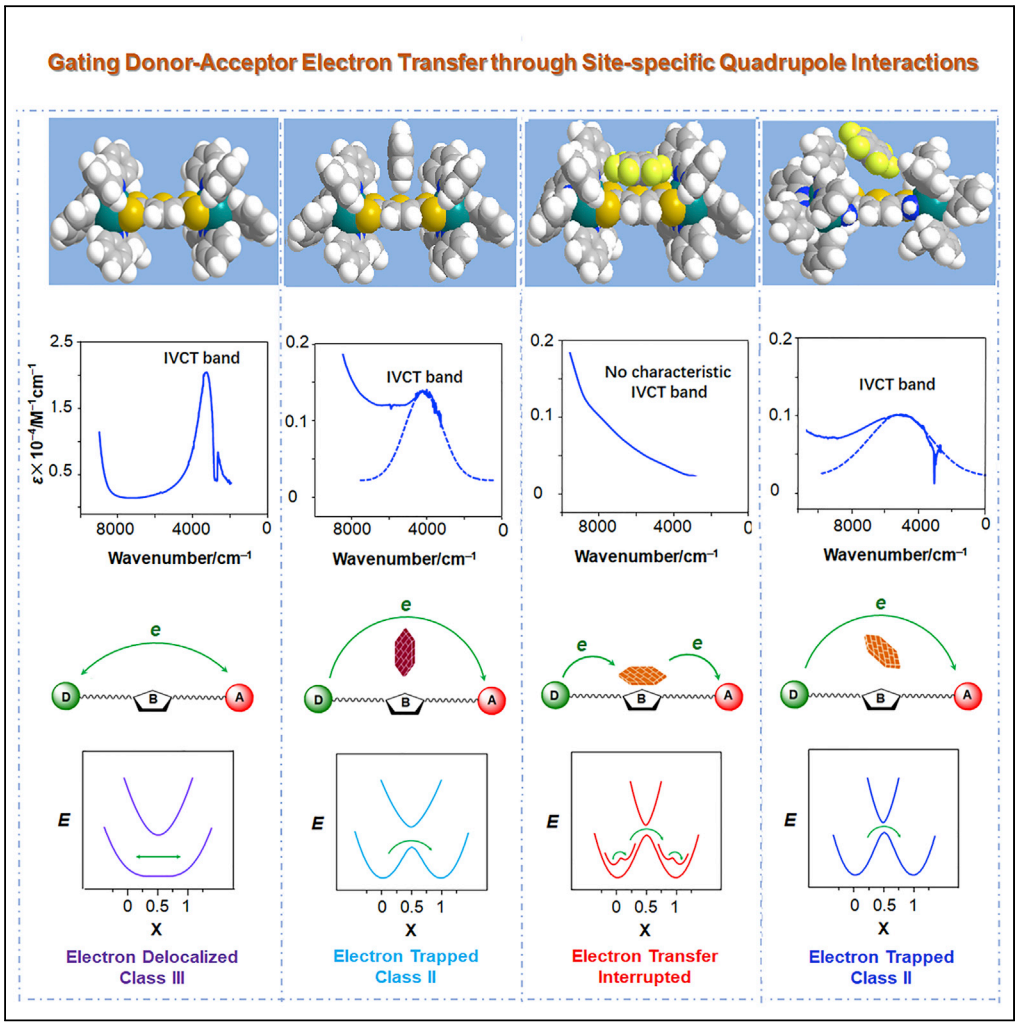


Suman Mallick, Lijiu Cao, Xiaoli Chen, ..., Ying Ning Tan, Tao Cheng, Chun Y. Liu

tcyliu@jnu.edu.cn

## HIGHLIGHTS

Electron transfer in {[$Mo_2$]-$C_4H_2S$-[$Mo_2$]}$^+$ is studied optically in aromatic solvents

Inclusion of a quadrupolar guest molecule gates the donor-acceptor electron transfer

Constitutional, electronic, and energetic complementarities in supramolecular system

Mallick et al., iScience 22, 269–287
December 20, 2019 
https://doi.org/10.1016/j.isci.2019.11.020

iScience

CellPress

Article

# Mediation of Electron Transfer by Quadrupolar Interactions: The Constitutional, Electronic, and Energetic Complementarities in Supramolecular Chemistry

Suman Mallick,[1,2] Lijiu Cao,[1,2] Xiaoli Chen,[1] Junpeng Zhou,[1] Yi Qin,[1] Gang Yi Wang,[1] Yi Yang Wu,[1] Miao Meng,[1] Guang Yuan Zhu,[1] Ying Ning Tan,[1] Tao Cheng,[1] and Chun Y. Liu[1,3,*]

## SUMMARY

**Studies of intermolecular interactions enhance our knowledge of chemistry across molecular and supramolecular levels. Here, we show that host-guest quadrupolar interaction has a profound influence on the molecular system. With covalently bonded dimolybdenum complex units as the electron donor (D) and acceptor (A) and a thienylene group ($C_4H_2S$) as the bridge (B), the mixed-valence D-B-A complexes are shaped with clefts in the middle of the molecule. Interestingly, in aromatic solvents, the D-A electronic coupling constants ($H_{ab}$) and electron transfer rates ($k_{et}$) are dramatically reduced. Theoretical computations indicate that an aromatic molecule is encapsulated in the cleft of the D-B-A array; quadrupole-quadrupole interaction between the guest molecule and the $C_4H_2S$ bridge evokes a charge redistribution, which increases the HOMO-LUMO energy gap, intervening in the through-bond electron transfer. These results demonstrate that a supramolecular system is unified underlying the characteristics of the assembled molecules through constitutional, electronic, and energetic complementarities.**

## INTRODUCTION

Electron transfer (ET) is one of the most fundamental chemical reactions, which is ubiquitous in chemical, biological, and physical systems (Balzani, 2001). Understanding and control of ET reactions has inspired intense theoretical and experimental studies for many decades (Creutz, 1983; Newton, 1991; Demadis et al., 2001), which have resulted in enormous achievements that benefit the developments of multiple disciplines as well as their intersection areas (Marcus, 1993; Migliore et al., 2014). The classical theoretic framework of ET was shaped in the 1960s, of which the core is the Marcus theory (Marcus, 1956, 1964, 1993). The Marcus ET theory is formulated with three independent energetic quantities, the free energy change ($\Delta G^\circ$), the reorganization energy ($\lambda$), and the electronic coupling (EC) matrix element ($H_{ab}$). In the condensed phase, reorganization energy for ET is determined by two factors, nuclear vibrations of the reactant and motions of the solvent molecules, which split $\lambda$ into two terms $\lambda_i$ (vibrational) and $\lambda_o$ (solvent) (Marcus, 1964, 1993; Marcus and Sutin, 1985), i.e., $\lambda = \lambda_i + \lambda_o$. In this context, for a given ET system, solvent effects play a critical role in governing the ET dynamics and kinetics (Rossky and Simon, 1994; Glover et al., 2010; Kubiak, 2013). However, not only do solvents affect an ET reaction through dipole solvation, which is modeled by the dielectric continuum theory (Marcus, 1956, 1964; Marcus and Sutin, 1985; Chen and Meyer, 1998), but solvent molecule may also cause an intramolecular charge redistribution or alter the ET process by site-specific interactions with the solute molecules. For $Ru^{2+}(NH_3)_5$-pyrazine in acidic solution, the red shift of metal (Ru) to ligand (pyrazine) charge transfer (MLCT) band from 21,000 to 19,000 $cm^{-1}$ was observed (Ford et al., 1968), which is attributed to the formation of hydrogen bonding derivative $Ru^{2+}(NH_3)_5$-pyrazine-$H^+$ from theoretical investigations (Zeng et al., 1996). Meyer and co-workers studied the solvent-induced intramolecular ET or change in the extent of electronic delocalization in the mixed-valence ions $[(bpy)_2ClOs(L)Ru(NH_3)_5]^{4+}$ (bpy = 2,2′-bipyridine; L = 4,4′-bipyridine [4,4′-bpy] or pyrazine [pz]) (Hupp et al., 1986; Neyhart et al., 1996). Recent work showed that polar solvent molecules intervening between the electron donor and acceptor can facilitate electron tunneling through a space (Chakrabarti et al., 2009; Graff et al., 2016). Similarly, in biological systems, it is found that interfacial water molecules are able to enhance the EC and accelerate interprotein ET (Miyashita et al., 2005; Lin et al., 2005). In the study of U-shaped donor (D)-bridge (B)-acceptor (A) molecular systems, Zimmt (Han and Zimmt, 1998;

[1]Department of Chemistry, Jinan University, 601 Huang-Pu Avenue West, Guangzhou 510632, China

[2]These authors contributed equally

[3]Lead Contact

*Correspondence: tcyliu@jnu.edu.cn

https://doi.org/10.1016/j.isci.2019.11.020

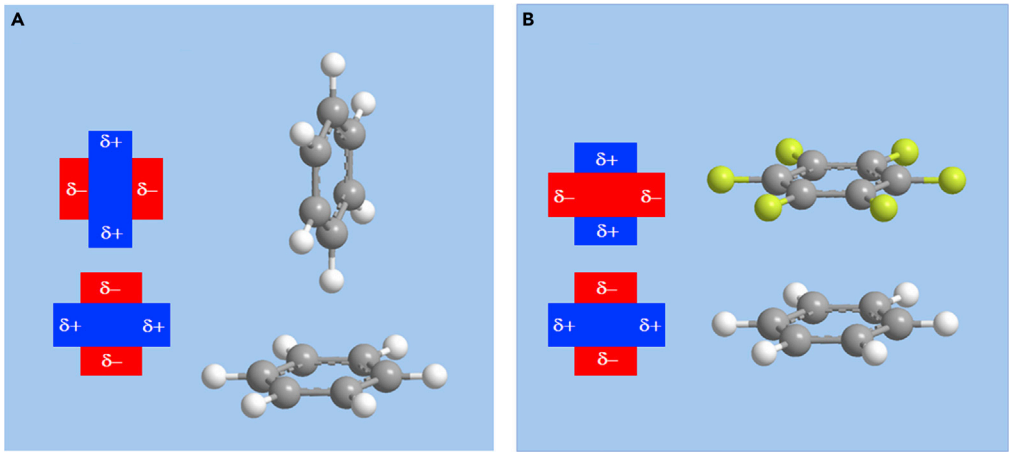


**Figure 1. Quadrupole-Quadrupole Interactions between Aromatic Molecules**

(A and B) Schematic representations of charge distribution and supramolecular conformations that maximize the electrostatic interaction energy between molecular electric quadrupole moments for an assemblage of benzene/benzene dimer (A) and benzene/hexafluorobenzene adduct (B).

Read et al., 1999) and Paddon-Row (Napper et al., 2002; Paddon-Row, 2003) have reported that the D-A electronic coupling is significantly enhanced in aromatic solvents. These unusual solvent effects are rationalized by inclusion of solvent molecule(s) in the cleft of the solute, which increases the electron tunneling efficiency; mechanistically, this EC phenomenon is referred to as "solvent-mediated superexchange coupling" (Han and Zimmt, 1998; Read et al., 1999; Napper et al., 2002; Paddon-Row, 2003; Kumar et al., 1996).

Aromatic solvents usually have zero or small dipole moments but large quadrupole moment. A quadrupole moment can be thought of as two dipole moments aligned in such a way that there is no net dipole (Dougherty, 1996). Benzene and hexafluorobenzene are the paradigms of quadrupolar molecules (Hunter et al., 2001; Williams, 2002). As shown in Figure 1, inverse charge distributions on the $C_6$ ring plane and edge are found for molecules $C_6H_6$ and $C_6F_6$ due to the opposite bond polarities for the C-H and C-F bonds, which endow the molecules with a large quadrupole moment with opposite signs, ca. $-29.0 \times 10^{-40}$C $m^2$ for benzene and $31.7 \times 10^{-40}$C $m^2$ for hexafluorobenzene (Williams, 2002). Therefore, to maximize the Coulomb interactions, the $C_6H_6$-$C_6H_6$ dimer adopts a T-shaped (edge to face) (Figure 1A) geometry, whereas the $C_6H_6$-$C_6F_6$ adduct is formed with a sandwich (face to face) (Figure 1B) configuration (Williams, 2002; Lee et al., 2007). A survey of protein structures showed that T-shape or the close geometries are preferred for the aromatic-aromatic interactions in proteins (Burley and Petsko, 1985). In metalloproteinase (Finzel et al., 1998), a face-to-face interaction was found between Tyr155 and the pentafluorophenyl group of the 1,3,4-thiadiazole-2-thione inhibitor. Theoretical work predicts that the T-shaped benzene dimer (Lee et al., 2007) has a binding energy of 2.4–2.5 kcal $mol^{-1}$ and the $C_6H_6$-$C_6F_6$ pair (West et al., 1997) is stabilized by 3.7 kcal $mol^{-1}$. Quadrupole-quadrupole interaction, as a type of strong intermolecular interactions, has been employed to construct supramolecular arrays or ordered structures (Williams, 2002; Ponzini et al., 2000). Relating to the ET study of synthetic D-B-A systems, aromatic structural motifs are frequently used as bridges in the molecular architecture. For an ET system involving aromatic $\pi$ moieties and operating in aromatic solvents, local quadrupole-quadrupole interactions may have significant impacts on solvation of the ET dynamics (Han and Zimmt, 1998; Read et al., 1999; Napper et al., 2002; Paddon-Row, 2003), which needs to be better understood.

In fact, the impact of site-specific solvation on ET dynamics raises important issues on fundamental chemistry: the constitutional, electromagnetic, energetic, and functional complementarities between the host and the guest molecules as well as the complementarities between these domains at the supramolecular molecular level. Supramolecular chemistry is aimed at providing general knowledge of host-guest molecular systems (Steed and Atwood, 2009) and now is moving forward to establish rules or regulations—adaptive chemistry toward the development of more complex, functional matters (Lehn, 2002). According to J.-M. Lehn, adaptive chemistry plays the role of bridging the chemical entities involving only covalent bonds

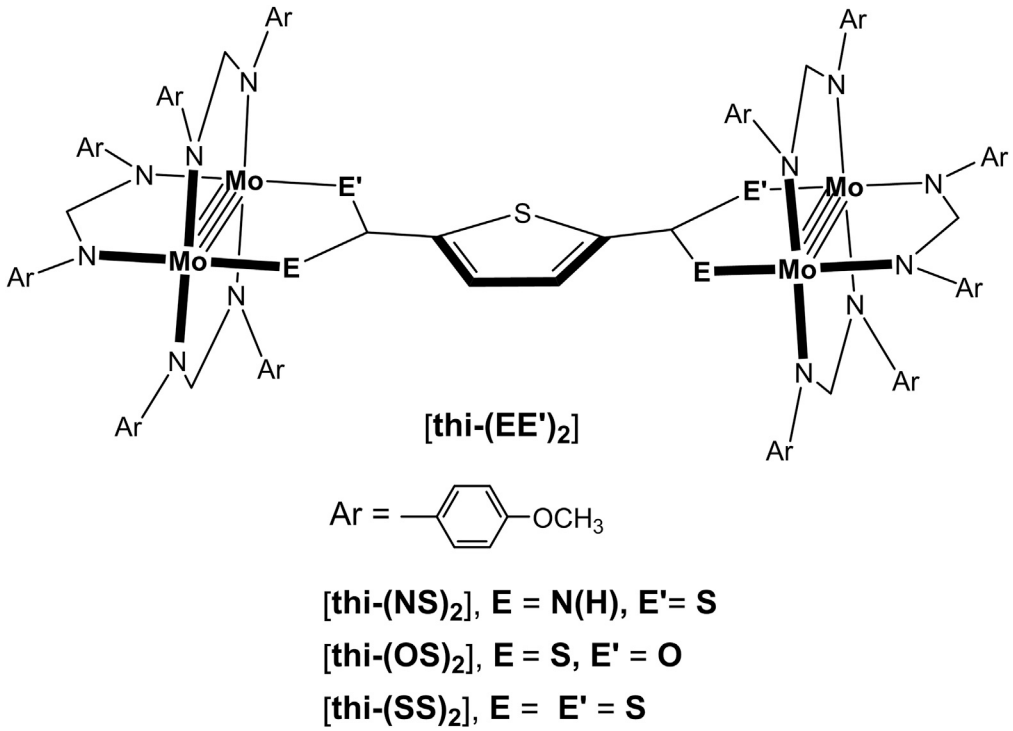


**Figure 2. A Molecular Scaffold for the $Mo_2$ Dimeric Complexes under Investigation**

By alternation of the chelating atoms of the thienyl dicarboxylate ligand from O to S, the electronic coupling between the donor and acceptor in the mixed-valence complexes can be significantly enhanced. The vertical aryl formamidinate ligands on the $Mo_2$ units, combining with the bridging ligand, create two inverse U-shaped clefts on the top and bottom in the middle of the molecule.

(molecules) and those involving covalent and non-covalent bonds (supramolecules) (Lehn, 2007). Following this direction, the challenge would be how to unify a supramolecular system with discrete structural and electronic identities into one system through complementary chemistry to function differently or more efficiently. Complementary chemistry is well exemplified in nature by the unique double helix structures of DNA and its unreplaceable functionality, developed from the aromatic base pairs through non-covalent $\pi$-$\pi$ interactions and hydrogen bonding (Calladine et al., 2004). The understandings on aromatic interactions can also be of particular importance in biological systems in which aromatic molecules and residues, such as tyrosine (Tyr), tryptophan (Trp), and phenylalanine (Phe) side chains, are widely spread (Burley and Petsko, 1985; Tatko and Waters, 2002). Strong local interactions between the aromatic side chains are the driving force for molecular recognition and self-organization, which controls the biochemical redox reactions or transport of electrons from one subunit to another (Meyer et al., 2003; Shih et al., 2008). Theoretical and experimental model systems have proven to be informative for interrogating the role of aromatic interactions (Waters, 2002; Thomas et al., 2002a, 2002b; Chen et al., 2012).

In this study, a series of three symmetrical $Mo_2$ dimers bridged by a thienylene ($C_4H_2S$) group, $[Mo_2(DAniF)_3]_2(\mu$-N(H)SC($C_4H_2S$)CN(H)S) (DAniF = *N,N′*-di(*p*-anisyl)formamidinate), $[Mo_2(DAniF)_3]_2(\mu$-OSC($C_4H_2S$)COS), and $[Mo_2(DAniF)_3]_2(\mu$-SSC($C_4H_2S$)CSS), designated as, **[thi-(NS)$_2$]**, **[thi-(OS)$_2$]**, and **[thi-(SS)$_2$]**, respectively, were synthesized and characterized crystallographically. Given a general formula $[Mo_2]$-$C_4H_2S$-$[Mo_2]$, the three $Mo_2$ dimers share a common thienylene bridge –(2,5-$C_4H_2S$)– but differ in the complex units $[Mo_2]$ by alternation of the ligating atoms of the bridging ligands from N to O and S, as shown in Figure 2, which modifies the electronic property of the $[Mo_2]$ donor (or acceptor) in the mixed-valence (MV) complexes to tune the EC. In the preliminary communication (Wu et al., 2017), we have shown that the three MV complexes implement a systematic transition from Class II to Class III via Class II-III in the Robin-Day's scheme (Robin and Day, 1967), which has been a challenge in mixed-valence chemistry (Demadis et al., 2001; Brunschwig et al., 2002; Concepcion et al., 2007). This series also exhibits typical dipole solvation dynamics, as indicated by the variation of intervalence charge transfer (IVCT)

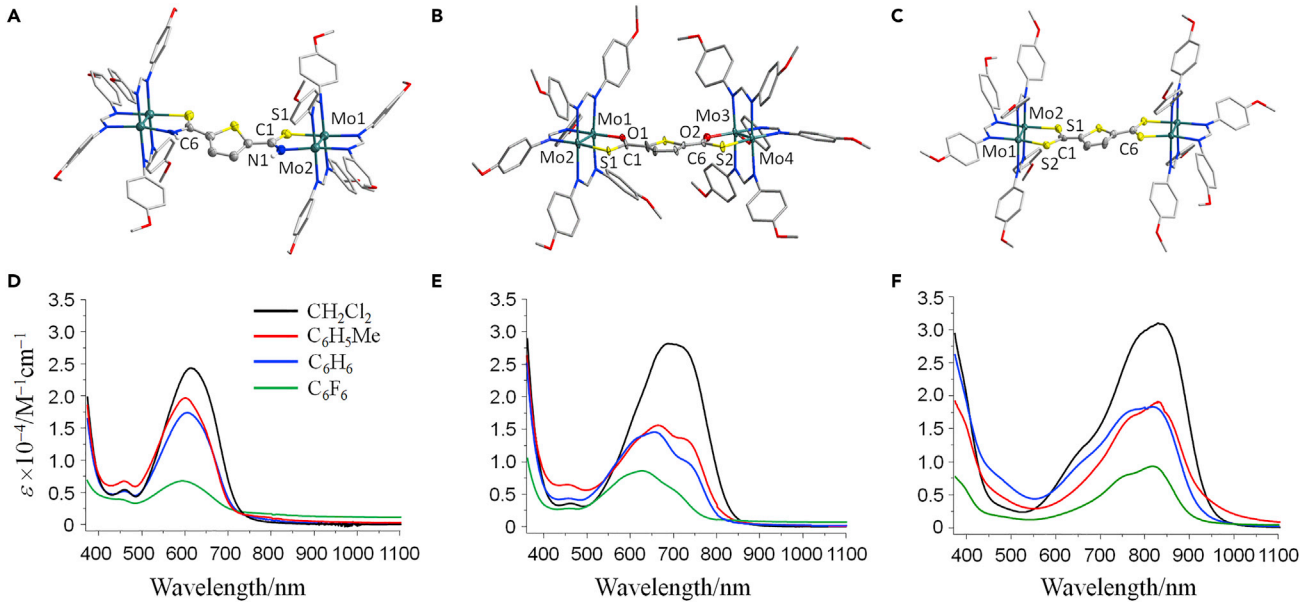


**Figure 3. X-ray Crystal Structures and Electronic Spectra of the $Mo_2$ Dimers**

(A–C) Single-crystal XRD structures of [**thi-(NS)$_2$**] (A), [**thi-(OS)$_2$**] (B), and [**thi-(SS)$_2$**] (C). Displacement ellipsoids for the core structure are drawn at the 40% probability level. Hydrogen atoms are omitted for clarity.

(D–F) Electronic spectra of [**thi-(NS)$_2$**] (D), [**thi-(OS)$_2$**] (E), and [**thi-(SS)$_2$**] (F) in dichloromethane (black), toluene (red), benzene (blue), and hexaflurobenzene (green).

characteristics (Wu et al., 2017). However, in this study, it is found that, in aromatic solvents with zero or small dipole moments, such as, toluene, benzene, and hexafluorobenzene, the EC strength and ET rates for the MV series are dramatically diminished. The electronic decoupling effects vary depending on the subtle differences of the [$Mo_2$]-$C_4H_2S$-[$Mo_2$] architectures and the magnitude of the effective quadrupolar moment $\langle Q \rangle$ of the solvents (Reynolds et al., 1996). These results are in sharp contrast to the solvent effects observed in the U-shaped organic D-B-A molecules in aromatic solvents, where inclusion of an aromatic molecule enhances the electronic coupling (Han and Zimmt, 1998; Read et al., 1999; Napper et al., 2002; Paddon-Row, 2003). Space filling models and density functional theory (DFT) calculations reveal that, in these systems, a solvent molecule (SM) is able to occupy the cleft between the two [$Mo_2$] units, forming an SM-included supramolecular entity, and mediate the ET process through quadrupole interactions between the SM and the thienylene ($C_4H_2S$) bridge. The quadrupole-quadrupole interaction results in mixing of the $\pi$ orbitals of the bridging ligand and the guest molecule, consequently increasing the highest occupied molecular orbital (HOMO)-lowest unoccupied molecular orbital (LUMO) energy gap and substantially attenuating or mediating the through-bond superexchange pathway.

## RESULTS

### Molecular Structures of the [$Mo_2$]-$C_4H_2S$-[$Mo_2$] Complexes

Three $Mo_2$ dimers, [$Mo_2$(DAniF)$_3$]$_2$($\mu$-N(H)SC($C_4H_2S$)CN(H)S) (DAniF = *N,N′*-di(*p*-anisyl)formamidinate) ([**thi-(NS)$_2$**]), [$Mo_2$(DAniF)$_3$]$_2$($\mu$-OSC($C_4H_2S$)COS) ([**thi-(OS)$_2$**]), and [$Mo_2$(DAniF)$_3$]$_2$($\mu$-SSC($C_4H_2S$)CSS) ([**thi-(SS)$_2$**]), were synthesized by assembling two quadruply-bonded $[Mo_2]^+$ complex units with a thiolated 2,5-thienylenedicarboxamidate and 2,5-thienylenedicarboxylate bridging ligand according to the published procedures (Wu et al., 2017). The molecular structures were determined by single-crystal X-ray diffraction, as shown in Figures 3A–3C; the crystallographic data and selected bond parameters are presented in Tables S1 and S2, respectively. The Mo−Mo bond distances of ~2.10 Å are in agreement with those of the quadruply bonded $Mo_2$ cores in similar ligand environments (Xiao et al., 2013; Shu et al., 2014; Tan et al., 2017). The Mo−N, Mo−O, and Mo−S bond lengths in these complexes are comparable with those in the thiooxamidate (Cotton et al., 2007) and thiooxalate (Tan et al., 2017) bridged analogues. In [**thi-(NS)$_2$**] and [**thi-(OS)$_2$**], the chelating atoms N(O) and S on the bridging ligands are positioned in *cis* arrangement with respect to the thienylene bridge (Figures 3A–3C), unlike the phenylene bridged analogues, which have the different chelating atoms of the bridging ligands in *trans* positions (Xiao et al.,

2013; Shu et al., 2014). It is worth noting that, in [**thi-(OS)$_2$**], the two S chelating atoms are situated away from the S atom of the $C_4H_2S$ group, whereas in [**thi-(NS)$_2$**], the three S atoms are on the same side. The different arrangements of the S atoms in [**thi-(OS)$_2$**] and [**thi-(NS)$_2$**] are ascribable to the different sizes of the chelating atoms O, S, and the NH groups. Furthermore, in [**thi-(OS)$_2$**] and [**thi-(SS)$_2$**], the central thienylene group is almost coplanar with the Mo−Mo bond vectors, with torsion angles of <10°; however, in [**thi-(NS)$_2$**], the central $C_4H_2S$ ring is deviated from the five-membered $Mo_2$ chelating rings by ~27°. Apparently, the non-co-planarity of this molecule is caused by the steric hindrance of the amidate hydrogen (N-*H*). These compounds and the other reported $Mo_2$ dimers having DAniF auxiliary ligands (Xiao et al., 2013; Shu et al., 2014; Tan et al., 2017) share the same molecular scaffold, which may be described topologically by an architecture with two inverse U-shaped clefts on the top and bottom in the middle of the molecule (Figure 2). The U-shaped clefts are shaped with a width of ~10 Å and a depth of ~8 Å, about 1 Å narrower than those for the phenylene analogues (Shu et al., 2014), because of the reduced size of the bridge. Geometrically, the three [$Mo_2$]-$C_4H_2S$-[$Mo_2$] complexes are slightly different with respect to the size and shape of the clefts (Table 1). For example, the clefts in [**thi-(OS)$_2$**] may be described more precisely as a "V" shape with a wide open in the front and a narrow one in the back, different from those for the other two molecules (Figures 3A–3C) because of the atomic size difference between S and O atoms. However, the X-ray structure may not represent the range of structures or conformations available in fluid solution environment.

### Electrochemistry and Spectroscopy of the $Mo_2$ Dimers in Dipole and Quadrupole Solvents

For the three $Mo_2$ dimers, electrochemical cyclic voltammograms (CVs) and differential pulse voltammograms (DPVs) were measured in dichloromethane (DCM) and toluene ($C_6H_5Me$); the CV diagrams are shown in Figure S1. In DCM, all three complexes display two reversible redox couples in the CVs, corresponding to the one-electron oxidations of the two $Mo_2$ centers from $Mo_2$(IV) to $Mo_2$(V). The redox potential separations ($\Delta E_{1/2}$) were measured from the peak-to-peak values in the DPVs to be 118, 184, and 348 mV (Ag/AgCl) for [**thi-(NS)$_2$**], [**thi-(OS)$_2$**], and [**thi-(SS)$_2$**], respectively. In the series, the differences in $\Delta E_{1/2}$ are extraordinary considering the very similar molecular and electronic structures between the complexes. Given the similar coordination environments for the $Mo_2$ centers and $Mo_2$•••$Mo_2$ distances, which diminish the differences in electrostatic effects, the magnitude of $\Delta E_{1/2}$ reflects the relative EC strength of the compound in the series. Therefore, the $\Delta E_{1/2}$ values of this series in DCM confirm the conclusion that chelating atoms on the bridging ligand enhance the EC effect in the order of N < O < S (Xiao et al., 2013; Shu et al., 2014; Tan et al., 2017). The fully thiolated [**thi-(SS)$_2$**] exhibits an exceptionally large $\Delta E_{1/2}$ (348 mV), signaling a very strong EC between the two [$Mo_2$] units in the MV state. Interestingly, for the series in toluene (Figure S2), the CV waves for the two one-electron redox processes are coalesced, giving $\Delta E_{1/2}$ values 115 mV ([**thi-(NS)$_2$**]), 74 mV ([**thi-(OS)$_2$**]), and 78 mV ([**thi-(SS)$_2$**]). These results indicate that, in toluene, the EC of the complexes is greatly reduced. It is surprising that the weakly coupled [**thi-(NS)$_2$**] exhibits the largest $\Delta E_{1/2}$, whereas similar and relatively small $\Delta E_{1/2}$ values are found for the two analogues that exhibit strong coupling in DCM. There are two major factors, resonant and electrostatic effects, that account for the potential separation $\Delta E_{1/2}$ in the MV complexes (Creutz, 1983; Crutchley, 1994). The diminished electronic decoupling in toluene should be attributed to a decrease of the resonant effect in that in a less polar solvent, the electrostatic effect is expected to increase.

Each of the $Mo_2$ dimers exhibits two absorption bands in the spectral region of 400–1,000 nm, as shown in Figures 3D–3F. The high energy (~450 nm), weak absorbance arises from vertical transition of the valence electrons of the $Mo_2$ center from the bonding orbital (δ) to the antibonding orbital (δ*) (Cotton et al., 2005). The intense, asymmetric, or overlapped absorptions can be assigned to metal (δ) to bridging ligand (π*) charge transfer (MLCT) according to the literature work (Xiao et al., 2013; Cotton et al., 2003; Chisholm et al., 2005). In the spectra, the MLCT energies ($E_{ML}$) decrease and intensities increase when the chelating atoms change from N to O to S (Table 1), parallel to the phenylene bridged series (Xiao et al., 2013; Liu et al., 2013). Provided with the well-defined MLCT absorptions in the [$Mo_2$]-bridge-[$Mo_2$] systems, together with the bridging ligand to metal charge transfer (LMCT) bands for the MV complexes, we have verified the distant (Zhu et al., 2016), conformational (Kang et al., 2016; Chen et al., 2018), and conjugational (Gao et al., 2019) dependences of the superexchange (McConnell, 1961; Creutz et al., 1994) ET under the semi-classical theoretical framework. For [**thi-(OS)$_2$**] and [**thi-(SS)$_2$**] in the quadrupolar solvents, the MLCT band profiles are apparently changed and the intensity is lowered, in comparison with the spectra in DCM. Particularly, for [**thi-(OS)$_2$**] and [**thi-(NS)$_2$**], the asymmetrical MLCT bands in DCM split into two overlapped bands in the aromatic solvents, indicating considerable modification of the electronic structure. Dramatic spectral variation is found for complexes in hexafluorobenzene, whereas in benzene and toluene the spectra are similar.

For instance, for [**thi-(OS)$_2$**], the MLCT band at 680 nm in DCM is shifted to 625 nm in $C_6F_6$ with a much lower molar extinction coefficient. For [**thi-(NS)$_2$**], however, the MLCT band profile is similar to that in DCM (Figure 3), showing weak solvent effects, which is consistent with the electrochemical results. Collectively, these results state that the aromatic solvent effects on the MLCT spectra are determined by the bilateral natures of the solvent and complex. Notably, the spectral differences in the aromatic solvents are even more pronounced than in strong dipole solvents, such as THF, acetone, and acetonitrile (Figure S3 and Table S3). Although the spectral variation in dipolar solvents is understood from the dielectric continuum theory (Marcus, 1956, 1964; Marcus and Sutin, 1985; Chen and Meyer, 1998), the physical origin for the spectral variation in the nonpolar solvents needs to be rationalized.

## Supramolecular Space-Filling Models Developed Based on the Geometrical and Electrostatic Complementarities

Having the U-shaped clefts in the structures (Figures 3A–3C), the $Mo_2$ complex molecules are capable of accommodating two small guest molecules. Topologically, the sizes and shapes of the clefts are compatible with the aromatic solvent molecules. On the other hand, the thienylene bridging moiety of the $Mo_2$ dimers, like a $C_6H_6$ ring (Figure 1), has negative charge distributed over the $C_4H_2S$ plane but is positive on the edge. The geometric and electrostatic complementarities of the complexes with the quadrupolar solvents lead us to propose a supramolecular system with a solvent molecule included in the cleft, similar to the reported U-shaped organic systems (Han and Zimmt, 1998; Read et al., 1999; Napper et al., 2002; Paddon-Row, 2003; Kumar et al., 1996). Presumably, the quadrupole-quadrupole interactions between the $C_4H_2S$ moiety and the included aromatic molecule endow the complex system with unusual electrochemical and spectroscopic (Figures 3D–3F) properties. In light of this, host-guest models are built for the complexes in each of the solvents. In addition, it is assumed that, for each of these supramolecular entities, only one solvent molecule is included, although there are two clefts available, because inclusion of one solvent molecule reduces the affinity of the complex to the second solvent molecule. To maximize the host-guest electrostatic attractions, for benzene and toluene, the solvent molecule contacts the $C_4H_2S$ group in a T-shaped geometry, whereas for hexafluorobenzene, a sandwich structure of $C_6F_6/C_4H_2S$ is adopted (Hunter et al., 2001; Williams, 2002). Furthermore, to reduce the computational expense, in these models, the auxiliary ligands are changed to *N,N′*-diphenylformamidinate or DPhF from DAniF of the complexes. For the three $Mo_2$ dimers in the three different quadrupolar solvents, there are nine host-guest entities, namely, [**thi-(NS)$_2$**]$\subset C_6H_6$, [**thi-(OS)$_2$**]$\subset C_6H_6$, and [**thi-(SS)$_2$**]$\subset C_6H_6$ for the complexes in benzene; [**thi-(NS)$_2$**]$\subset C_6H_5Me$, [**thi-(OS)$_2$**]$\subset C_6H_5Me$, and [**thi-(SS)$_2$**]$\subset C_6H_5Me$ in toluene; and [**thi-(NS)$_2$**]$\subset C_6F_6$, [**thi-(OS)$_2$**]$\subset C_6F_6$, and [**thi-(SS)$_2$**]$\subset C_6F_6$ in hexafluorobenzene.

These 1:1 models are optimized at the density functional level to reach the energy minimum of the supramolecular systems, by which the corresponding space-filling models are developed. As shown in Figures 4A–4C, for each of the space-filling models, the aromatic molecule is held in one of the clefts of the complex molecule in the expected orientation. The $C_6H_5Me$ or $C_6H_6$ molecule in the cleft stands vertically on the $C_4H_2S$ plane (edge to face) with a centroid distance of 5.3–6.9 Å (Figure S4), showing a typical CH$\cdots\pi$ quadrupolar interaction (Hunter et al., 2001; Nishio, 2004). The ring-ring distances between the host and guest molecules are in agreement with the computed interactions between the corresponding free arenes reported elsewhere (Singh et al., 2009) and fall in the range of 4.5–7.0 Å for aromatic-aromatic interactions in proteins (Burley and Petsko, 1985). The $C_6F_6$-$C_4H_2S$ distances in [**thi-(OS)$_2$**]$\subset C_6F_6$ (4.1 Å) and [**thi-(SS)$_2$**]$\subset C_6F_6$ (4.0 Å) are comparable with 3.7 Å in the crystal structures of the $C_6H_6$-$C_6F_6$ adduct (Williams et al., 1992) and are in good agreement with the face-to-face interaction (3.8–4.0 Å) between Tyr155 and the pentafluorophenyl side chain of a metalloenzyme (Finzel et al., 1998). Owing to the large torsion angle (27°) of the $C_4H_2S$ bridge, the guest molecule in [**thi-(NS)$_2$**] is more than 1 Å further away, in comparison with systems [**thi-(OS)$_2$**] and [**thi-(SS)$_2$**], and the $C_6F_6$ molecule is tilted in the cleft (Figures 4A–4C and Table S2). The host-guest distances in [**thi-(OS)$_2$**]$\subset$SM are slightly longer than those in [**thi-(SS)$_2$**]$\subset$SM because of the subtle geometric differences of the clefts (Figure S4). Therefore, these space-filling models show the molecular signature of a "lock and key" relationship in supramolecular chemistry (Lehn, 2007).

## DFT Calculations on the Supramolecular Models

DFT calculations were performed on the supramolecular models, in comparison with the complex models. The complex structures are simplified by replacing the bulky anisyl groups on the auxiliary ligands with hydrogen atoms, yielding the computational models, [**thi-(NS)$_2$**]′, [**thi-(OS)$_2$**]′, and [**thi-(SS)$_2$**]′. Previous work has proven that the calculated results from the simplified models are in excellent agreement with

| Complex Model | DFT Calculation | | | | | | | Experiment | |
|---|---|---|---|---|---|---|---|---|---|
| | Distance (Å) | HOMO−1 (eV) | HOMO (eV) | LUMO (eV) | $\Delta E_{H-H-1}$ (eV) | $\Delta E_{H-L}$ ($cm^{-1}$) (nm) | $\Delta\Delta E_{H-L}$[a] (kcal $mol^{-1}$) | $\lambda_{ML}$ (nm) | $\Delta E_{ML}$[b] (kcal $mol^{-1}$) |
| [thi-$(NS)_2$]′ | – | −4.22 | −3.88 | −1.87 | 0.34 | 16,211 (617) | | 611 | |
| [thi-$(NS)_2$]′ ⊂$C_6H_5Me$ | 6.9 | −4.21 | −3.87 | −1.86 | 0.34 | 16,211 (617) | 0 | 598 | 1.0 |
| [thi-$(NS)_2$]′ ⊂$C_6H_6$ | 6.1 | −4.20 | −3.86 | −1.80 | 0.34 | 16,615 (602) | 1.2 | 602 | 0.7 |
| [thi-$(NS)_2$]′ ⊂$C_6F_6$ | 5.3 | −4.06 | −3.76 | −1.70 | 0.30 | 16,615 (602) | 1.2 | 591 | 1.6 |
| [thi-$(OS)_2$]′ | – | −4.35 | −3.99 | −2.22 | 0.36 | 14,276 (700) | | 680 | |
| [thi-$(OS)_2$]′ ⊂$C_6H_5Me$ | 5.4 | −4.28 | −3.95 | −2.08 | 0.33 | 15,082 (663) | 2.3 | 662 | 1.1 |
| [thi-$(OS)_2$]′ ⊂$C_6H_6$ | 5.3 | −4.26 | −3.94 | −2.04 | 0.32 | 15,324 (653) | 3.0 | 655 | 1.6 |
| [thi-$(OS)_2$]′ ⊂$C_6F_6$ | 4.1 | −4.14 | −3.84 | −1.83 | 0.30 | 16,211 (617) | 5.5 | 625 | 3.7 |
| [thi-$(SS)_2$]′ | – | −4.59 | −4.11 | −2.55 | 0.48 | 12,582 (795) | | 790 | |
| [thi-$(SS)_2$]′ ⊂$C_6H_5Me$ | 5.3 | −4.52 | −4.10 | −2.45 | 0.42 | 13,308 (751) | 2.1 | 770 | 0.9 |
| [thi-$(SS)_2$]′ ⊂$C_6H_6$ | 5.3 | −4.52 | −4.11 | −2.45 | 0.41 | 13,388 (747) | 2.3 | 760 | 1.4 |
| [thi-$(SS)_2$]′ ⊂$C_6F_6$ | 4.0 | −4.41 | −4.01 | −2.27 | 0.40 | 14,034 (713) | 4.1 | 750 | 1.9 |

**Table 1. DFT Calculated Frontier Molecular Orbital Energies for the Supramolecular Models in Comparison with the Spectral MLCT Data in $CH_2Cl_2$**

[a]$\Delta\Delta E_{H-L}$ refers to the difference of the HOMO-LUMO energy gap ($\Delta E_{H-L}$) for the complex in the given aromatic solvent relative to the $\Delta E_{H-L}$ in DCM.

[b]$\Delta E_{ML}$ refers to the difference of the metal to ligand charge transfer energy ($E_{ML}$) measured in the spectra for the complex in the given aromatic solvent relative to the $E_{ML}$ in DCM.

the experimental data (Xiao et al., 2013; Tan et al., 2017; Cotton et al., 2003). The computational models for the proposed supramolecular entities are constructed with a quadrupolar solvent molecule included in one of the clefts of the simplified complex models, corresponding to the space-filling models (Figures 4A–4C), which are [**thi-$(NS)_2$**]′⊂$C_6H_6$, [**thi-$(OS)_2$**]′⊂$C_6H_6$, and [**thi-$(SS)_2$**]′⊂$C_6H_6$ for the complexes in benzene; [**thi-$(NS)_2$**]′⊂$C_6H_5Me$, [**thi-$(OS)_2$**]′⊂$C_6H_5Me$, and [**thi-$(SS)_2$**]′⊂$C_6H_5Me$ in toluene; and [**thi-$(NS)_2$**]′⊂$C_6F_6$, [**thi-$(OS)_2$**]′⊂$C_6F_6$, and [**thi-$(SS)_2$**]′⊂$C_6F_6$ in hexafluorobenzene.

The optimized geometries of the simplified supramolecular models are essentially the same as those of the space-filling models regarding to the host-guest contacts. For [**thi-$(OS)_2$**]′, the resultant frontier molecular orbitals HOMO, HOMO−1, and LUMO are shown in Figure 4D, as a representative of the three complex systems (see Figures S6 and S7 for the rest systems), and the MO energies are presented in Table 1, along with experimental results. As shown in Figure 4D, the HOMO results from the out-of-phase (δ − δ) combination of the δ orbitals with a filled π orbital of the bridging ligand, whereas the HOMO−1 is obtained by in-phase (δ + δ) combination of the δ orbitals with an empty π* orbital of the bridging ligand. These two metal orbitals are nondegenerate owing to d(δ)-p(π) orbital interactions between the $Mo_2$ centers and the bridging ligand (Xiao et al., 2013; Tan et al., 2017). The LUMO is contributed mainly by the π* orbital of the bridging ligand. Remarkably, for supramolecular systems [**thi-$(OS)_2$**]′⊂SM (Figure 4D) and [**thi-$(SS)_2$**]′⊂SM (Figure S7), the guest molecule is involved in the LUMO by contributing significant π electron density (~6%), as a result, substantially raising the LUMO energy level, relative to that of the complex model. It is worth noting that, for both T-shaped and face-to-face interaction modes (Figure 4D), only the aromatic π orbital of the guest molecule is mixed with the π orbital of the bridging ligand. In the series, the LUMO

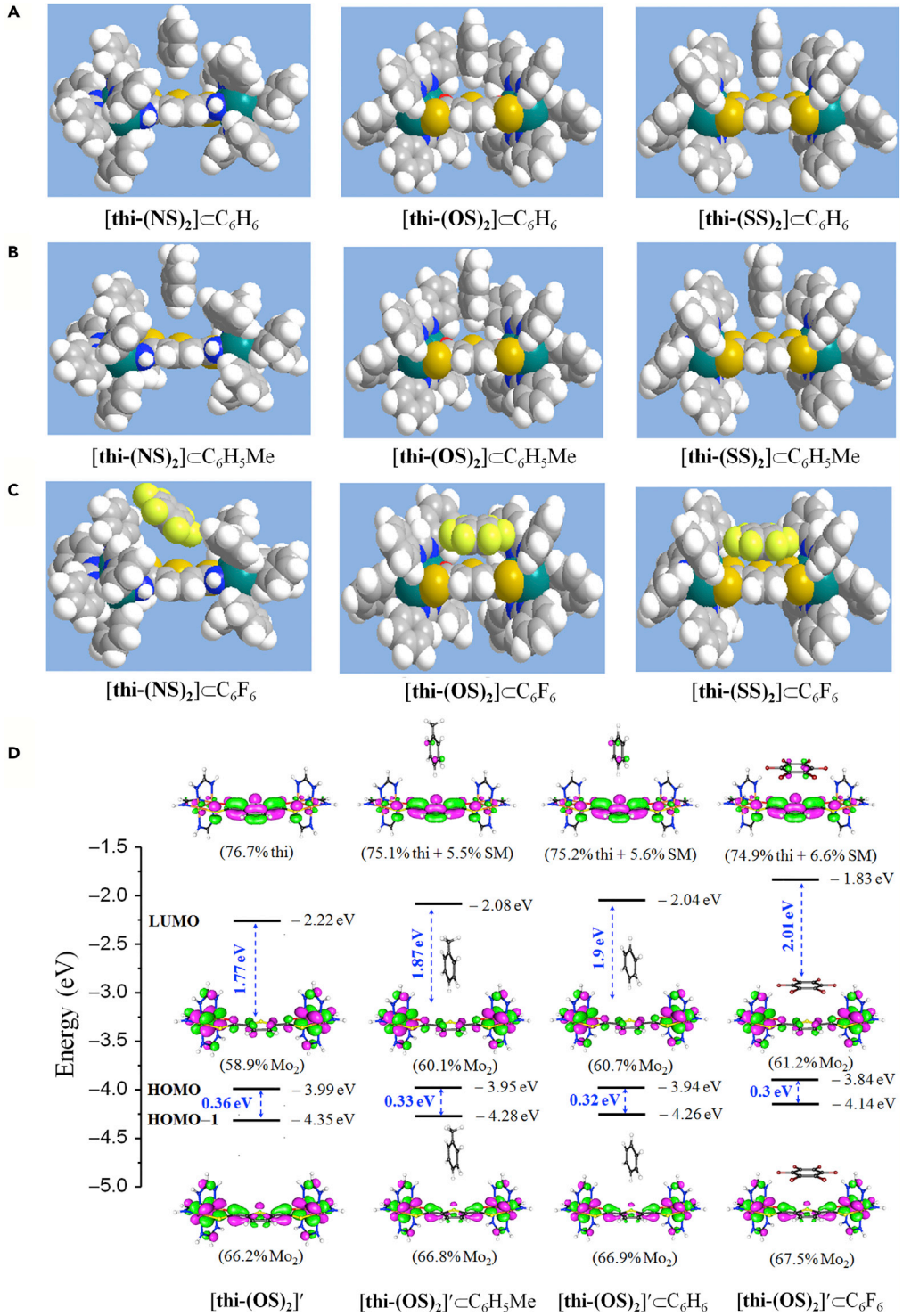


**Figure 4. Space-Filling Models and Frontier Molecular Orbitals Calculated on the Supramolecular Models**

(A–C) Energy-optimized space-filling models for the host-guest entities. For each of the systems, a solvent molecule is encapsulated in the U-shaped cavity of the $[Mo_2]$-$C_4H_2S$-$[Mo_2]$ molecule, where $[Mo_2] = [Mo_2(DPhF)_3]$, in T-shaped and sandwich manners for benzene (or toluene) and hexafluorobenzene, respectively, in contact with the thienylene group of the bridging ligand. The centroid distances between the host moiety ($C_4H_2S$) and guest molecules are presented in Figure S4. Geometric optimizations starting with different host-guest geometries reached the configurations without quadrupole-quadrupole interaction between the guest molecule and the $C_4H_2S$ group (Figure S5).

**Figure 4. *Continued***

(D) Frontier molecular orbitals (isodensity value ±0.02) for the simplified models [**thi-(OS)$_2$**]′, [**thi-(OS)$_2$**]′⊂$C_6H_5Me$, [**thi-(OS)$_2$**]′⊂$C_6H_6$, and [**thi-(OS)$_2$**]′⊂$C_6F_6$, shown along with the relative orbital energies, the HOMO−LUMO energy gaps and density contributions of metal center ($Mo_2$), bridging ligand (thi) and solvent molecule (SM) to the MOs. For series [**thi-(NS)$_2$**]′ and [**thi-(SS)$_2$**]′, these theoretical results are presented in Figures S6 and S7, respectively.

energy increases as a function of the strength of the quadrupole-quadrupole interactions (Table 1 and Figures S6 and S7). For instance, small LUMO energy variation is found for [**thi-(OS)$_2$**]′⊂$C_6H_5Me$ but large change for [**thi-(OS)$_2$**]′⊂$C_6F_6$ with strong quadrupole interactions. In contrast, Figure S6 shows that, for [**thi-(NS)$_2$**]′⊂SM, the included solvent molecule does not contribute electron density to the LUMO, although the MO energies are varied appreciably. The different solvation property of [**thi-(NS)$_2$**] should be attributed to the large host-guest distances and weak quadrupole effects, consistent with the experimental results. Calculations show clearly that the strong quadrupole-quadrupole interaction evokes charge redistribution, modifying the electronic structure of the bridging ligand. This means that intermolecular interaction is able to alter profoundly a chemical system.

In studies of the $Mo_2$ dimers, it is well documented that the HOMO to LUMO electron transition gives rise to the metal to ligand charge transfer absorption (Xiao et al., 2013; Tan et al., 2017; Cotton et al., 2003; Chisholm et al., 2005); therefore, the HOMO to LUMO energy gap ($\Delta E_{H\text{-}L}$) is transformed to the MLCT band energy ($E_{ML}$). Remarkably, for all the computational models, the calculated $\Delta E_{H\text{-}L}$ values (Table 1) are in good agreement with measured $E_{ML}$ from the UV-visible spectra (Figures 3D–3F). For those without a guest molecule included, which model the spectra of the complexes in DCM, the $\Delta E_{H\text{-}L}$ values decrease with changing the chelating atoms from N to O to S, consistent with the variation trend of $E_{ML}$ for the series. Importantly, for each of the three complex systems, the $\Delta E_{H\text{-}L}$ and $E_{ML}$ values (eV) increase as a result of introducing a quadrupole molecule into the cleft. For the complex in different solvents, the magnitudes of $\Delta E_{H\text{-}L}$ vary depending on the nature of the included quadrupole molecule (Table 1) and thus correlating to the strength of quadrupole-quadrupole interaction. In general, toluene has the smallest influence on the electronic and spectroscopic properties and hexafluorobenzene the largest, as expected from the effective quadrupole moments of the solvents, that is, $\langle Q \rangle = 7.92$ DÅ ($C_6H_5Me$) and 9.43 DÅ ($C_6F_6$) (Reynolds et al., 1996). The quadrupolar effect of benzene is generally larger than that in toluene, as measured from $\Delta E_{H\text{-}L}$ and $E_{ML}$ (Table 1), because of the larger $\langle Q \rangle$ (8.35 DÅ). For [**thi-(NS)$_2$**], the MLCT energies in the aromatic solvents are higher than those in DCM, showing some quadrupolar effects. It is noted that the $E_{ML}$ value in toluene (598 nm) is larger than that in benzene (602 nm), whereas the calculated electronic transition energy ($\Delta E_{H\text{-}L}$) for the benzene-included system is larger (Table 1). This is because the toluene guest molecule exerts weak quadrupolar effects relative to benzene plus a significant dipole solvation effect that is not accounted for in the calculations. Therefore, the computational results are in excellent agreement with the experimental results, showing the strength of quadrupole effects exactly as predicated by the space-filling models.

The HOMO−HOMO−1 gap ($\Delta E_{H\text{-}H\text{-}1}$) also measures the relative strength of EC between the two $Mo_2$ centers (Xiao et al., 2013; Tan et al., 2017; Cotton et al., 2007); large orbital splitting indicates a strong metal to metal interaction. In each complex system, the solvent-free model exhibits a $\Delta E_{H\text{-}H\text{-}1}$ value larger than those of the supramolecular systems. Therefore, the decrease of $\Delta E_{H\text{-}H\text{-}1}$ or $\Delta\Delta E_{H\text{-}H\text{-}1}$ value (Table 1) in aromatic solvent accounts for the quadrupolar effect. System [**thi-(NS)$_2$**]′ has the smallest variation of $\Delta E_{H\text{-}H\text{-}1}$ in aromatic solvents, thus experiencing the smallest impact from the aromatic guest. For [**thi-(OS)$_2$**]′ and [**thi-(SS)$_2$**]′, the changes in HOMO−HOMO−1 gap in the same solvent are similar, indicating similar solvent decoupling effects. The relatively weak quadrupolar effects for [**thi-(OS)$_2$**] is ascribable to the "V"-shaped geometry of the clefts in the molecular structure (Figure 3), which increases the host-guest centroid distances by 0.1 Å (Figure S4). Overall, DFT calculations on the complex models suggest that, in aromatic solvents, a solvent molecule included in the cleft of the [$Mo_2$]-$C_4H_2S$-[$Mo_2$] molecule impacts significantly the electronic configuration of the complex through quadrupole-quadrupole interactions with the $C_4H_2S$ group.

## Intervalence Charge Transfer Absorptions and the EC Parameters ($H_{ab}$) of the Mixed-Valence Complexes

The cationic mixed-valence complexes [**thi-(NS)$_2$**]$^+$, [**thi-(OS)$_2$**]$^+$, and [**thi-(SS)$_2$**]$^+$ were produced by oxidation of the neutral compounds with one equivalent of ferrocenium hexafluorophosphate (*in situ*) and characterized by X-band EPR spectra with a *g* value of ~1.95, as shown in Figure S8 (Wu et al., 2017; Xiao et al., 2013; Tan et al., 2017; Chisholm et al., 2005). The near-mid-IR spectra of the MV complexes in toluene, benzene, and hexafluorobenzene are shown in Figure 5 and the spectral parameters listed in Table 2, together

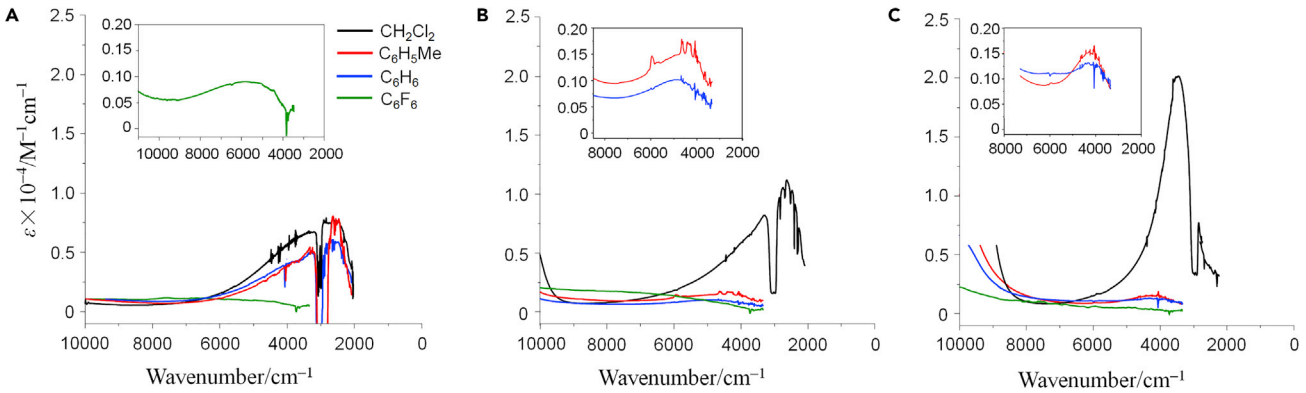


**Figure 5. Intervalence Charge Transfer Spectra of the Mixed-Valence Complexes in Various Solvents**

(A–C) IVCT absorptions in the near-mid-IR region of the MV complexes $[\mathbf{thi\text{-}(NS)_2}]^+$ (A), $[\mathbf{thi\text{-}(OS)_2}]^+$ (B), and $[\mathbf{thi\text{-}(SS)_2}]^+$ (C) in dichloromethane (black), toluene (red), benzene (blue), and hexafluorobenzene (green). Shown in the inset are the y-expanded IVCT bands for the complex in the given solvents. $[\mathbf{thi\text{-}(OS)_2}]^+$ and $[\mathbf{thi\text{-}(SS)_2}]^+$ in hexafluorobenzene do not display characteristic IVCT bands.

with data in DCM for comparison, and the full spectra are presented in Figures S9–S18. Importantly, in the aromatic solvents, the MV complexes exhibit distinct spectra from those in DCM, especially for $[\mathbf{thi\text{-}(OS)_2}]^+$ and $[\mathbf{thi\text{-}(SS)_2}]^+$, and the spectra in benzene and toluene are substantially different from those in hexafluorobenzene. For $[\mathbf{thi\text{-}(OS)_2}]^+$ and $[\mathbf{thi\text{-}(SS)_2}]^+$, characteristic IVCT absorptions are detected with increased transition energies ($E_{IT}$) and decreased molar extinction coefficients ($\varepsilon_{IT}$) (Table 2), relative to the IVCT bands in DCM, whereas in hexafluorobenzene, a very weak and broad IVCT absorbance is observed for the three MV complexes. These optical behaviors show the electronic decoupling effects of the aromatic solvents according to the Hush formalism (Hush, 1967, 1968), in sharp contrast to the organic U-shaped donor-acceptor systems, in which inclusion of an aromatic solvent molecule improves the EC (Han and Zimmt, 1998; Read et al., 1999; Napper et al., 2002; Paddon-Row, 2003; Kumar et al., 1996). Notably, the spectral variations in aromatic solvents are quite different from the observations in dipole solvents THF, acetone, and acetonitrile (Figure S19), which show solvent independence of the IVCT energy for electron delocalized systems of Class III (Wu et al., 2017; Tan et al., 2017).

Based on the IVCT band parameters ($E_{IT}$, $\varepsilon_{IT}$, and $\Delta\nu_{1/2}$) (Table 2), we can quantitatively evaluate the quadrupolar effects on electronic coupling by calculation of the EC matrix elements $H_{ab}$ using the Mulliken-Hush expression (Equation 1) (Creutz, 1983; Hush, 1967, 1968).

$$H_{ab} = 2.06 \times 10^{-2} \frac{\left(\Delta\nu_{1/2}\varepsilon_{max}E_{IT}\right)^{1/2}}{r_{ab}} \qquad \text{(Equation 1)}$$

For strongly coupled Class II-III and Class III, $H_{ab}$ is determined directly from $E_{IT}$ according to the semi-classical theory (Equation 2) (Creutz, 1983; Brunschwig et al., 2002),

$$H_{ab} = E_{IT}/2 \qquad \text{(Equation 2)}$$

In application of Equation 1, the effective ET distance $r_{ab}$ is estimated to be 5.3 Å from the geometrical length of the "$-CC_4H_2SC-$" moiety, considering electron delocalization within the $[Mo_2]$ unit (Wu et al., 2017; Xiao et al., 2013; Tan et al., 2017; Yu et al., 2016). In the previous communication (Wu et al., 2017), the $H_{ab}$ parameters in DCM were determined to be 892 ($[\mathbf{thi\text{-}(NS)_2}]^+$), 1,127 ($[\mathbf{thi\text{-}(OS)_2}]^+$), and 1,645 $cm^{-1}$ ($[\mathbf{thi\text{-}(SS)_2}]^+$). For the series, the IVCT characteristics and the large $H_{ab}$ values indicate that these MV complexes are moderately strongly or strongly coupled, thus being assigned to three different regimes, Class II, Class II-III, and Class III in Robin-Day's classification (Wu et al., 2017). In this study, for the MV complexes that exhibit well-defined IVCT bands in the aromatic solvents with the band parameters ($E_{IT}$, $\varepsilon_{IT}$, and $\Delta\nu_{1/2}$) determinable, we are able to derive the $H_{ab}$ parameters from Equation 1 (Table 2). In DCM, by featuring an intense, low-energy (2,254 $cm^{-1}$) and half cutoff IVCT band in the spectra (Figure 5B), $[\mathbf{thi\text{-}(OS)_2}]^+$ is characterized as a species on the Class II-III borderline (Demadis et al., 2001; Wu et al., 2017; Brunschwig et al., 2002). For the fully thiolated $[\mathbf{thi\text{-}(SS)_2}]^+$, the IVCT band energy ($E_{IT}$) is increased to 3,290 $cm^{-1}$ and the band shape is more symmetric, which manifests the Class II-III crossover to Class III (Wu et al., 2017; Tan et al., 2017). Importantly, in the aromatic solvents, the differences in EC between $[\mathbf{thi\text{-}(OS)_2}]^+$ and $[\mathbf{thi\text{-}(SS)_2}]^+$ are blurred and the two complexes exhibit similar IVCT characteristics, which are completely different from the spectra in DCM (Figures 5B and 5C). For

| System | $E_{IT}$ ($cm^{-1}$) | $\epsilon_{IT}$ ($M^{-1}cm^{-1}$) | $\Delta\nu_{1/2}$ (exp) ($cm^{-1}$) | $\Delta\nu_{1/2}$ (cal) ($cm^{-1}$) | $H_{ab}$ ($cm^{-1}$) | $2H_{ab}/\lambda$ | $\Delta G^{*}$ ($cm^{-1}$) | $k_{et}$ ($s^{-1}$) |
|---|---|---|---|---|---|---|---|---|
| $[thi\text{-}(NS)_2]^{+}$[a] | 2,630 | 7,933 | 2,480 | 2,464 | 892 | 0.68 | 68 | $3.6\times10^{12}$ |
| $[thi\text{-}(NS)_2]^{+}\subset C_6H_5Me$ | 2,062 | 7,760 | 1,845 | 2,176 | 668 | 0.65 | 64 | $3.7\times10^{12}$ |
| $[thi\text{-}(NS)_2]^{+}\subset C_6H_6$ | 2,365 | 5,085 | 2,242 | 2,337 | 638 | 0.54 | 125 | $2.7\times10^{12}$ |
| $[thi\text{-}(NS)_2]^{+}\subset C_6F_6$ | 5,745 | 913 | 4,255 | 3,632 | 580 | 0.20 | 915 | $6.0\times10^{10}$ |
| $[thi\text{-}(OS)_2]^{+}$[a] | 2,254 | 11,398 | 2,009 | 2,281 | 1,127 | 1.00 | 0 | $5.0\times10^{12}$ |
| $[thi\text{-}(OS)_2]^{+}\subset C_6H_5Me$ | 4,570 | 1,512 | 2,564 | 3,240 | 517 | 0.23 | 684 | $1.8\times10^{11}$ |
| $[thi\text{-}(OS)_2]^{+}\subset C_6H_6$ | 4,886 | 1,017 | 2,936 | 3,350 | 469 | 0.19 | 797 | $1.1\times10^{11}$ |
| $[thi\text{-}(OS)_2]^{+}\subset C_6F_6$ | / | / | / | / | / | / | / | / |
| $[thi\text{-}(SS)_2]^{+}$[a] | 3,290 | 20,261 | 1,266 | 2,823 | 1,645 | 1.00 | 0 | $5.0\times10^{12}$ |
| $[thi\text{-}(SS)_2]^{+}\subset C_6H_5Me$ | 4,238 | 1,523 | 2,055 | 3,120 | 448 | 0.21 | 659 | $2.1\times10^{11}$ |
| $[thi\text{-}(SS)_2]^{+}\subset C_6H_6$ | 4,246 | 1,305 | 2,358 | 3,122 | 444 | 0.21 | 664 | $2.0\times10^{11}$ |
| $[thi\text{-}(SS)_2]^{+}\subset C_6F_6$ | / | / | / | / | / | / | / | / |

**Table 2. Spectroscopic Data of the IVCT Bands and the Derived EC and ET Parameters for the MV Dimers $[thi\text{-}(NS)_2]^{+}$, $[thi\text{-}(OS)_2]^{+}$, and $[thi\text{-}(SS)_2]^{+}$ in Different Solvents**

[a]The IVCT band parameters are reported by Wu et al., 2017.

instance, for $[thi\text{-}(SS)_2]^{+}$ in toluene and benzene, the IVCT band energy is no longer solvent independent as in polar solvents (Figure S19). For both, a very weak, Gaussian-shaped IVCT band is observed and the maximum absorption shifted toward high energy. The transition energies for $[thi\text{-}(OS)_2]^{+}$, 4,570 $cm^{-1}$ in toluene and 4,886 $cm^{-1}$ in benzene, are significantly higher than those for $[thi\text{-}(SS)_2]^{+}$ in these solvents (Table 2). The larger $H_{ab}$ values for $[thi\text{-}(OS)_2]^{+}$ as compared with $[thi\text{-}(SS)_2]^{+}$ are in sharp contrast to observations that substitution of S atoms for the O chelating atoms greatly improves the EC between the two bridged $Mo_2$ centers (Xiao et al., 2013; Tan et al., 2017). Furthermore, in benzene and toluene, these two MV complexes exhibit the IVCT bands much narrower than those in dipole solvents (Table S4) (Wu et al., 2017) and those observed for other weakly coupled $\{[Mo_2]\text{-bridge-}[Mo_2]\}^{+}$ complexes in DCM (Xiao et al., 2013; Shu et al., 2014; Tan et al., 2017; Kang et al., 2016). This implies that the nature of the bridge is somehow altered, in accordance with the computational results (Figure 4D). The significant change of the IVCT band features indicates the tremendous *electronic decoupling effects* of the aromatic solvents. Quantitatively, the $H_{ab}$ values, ca. 450–520 $cm^{-1}$ (Table 2) are lowered to half or one-third of the values in DCM, indicating very weak EC, in comparison with the data for related $Mo_2$ D-B-A systems (Xiao et al., 2013; Shu et al., 2014; Tan et al., 2017; Kang et al., 2016). In hexafluorobenzene, the MV complexes experience very strong quadrupolar effects, displaying an extremely broad charge transfer absorption (Figure 5B), which does not characterize a classic double-well ET system (Creutz, 1983; Newton, 1991; Marcus, 1993; Marcus and Sutin, 1985).

Distinct optical properties are observed for $[thi\text{-}(NS)_2]^{+}$ in the aromatic solvents. In benzene and toluene, it exhibits intense asymmetrical IVCT spectra, with band parameters similar to those in DCM (Figure 5 and Table 2). The $H_{ab}$ values, 638 $cm^{-1}$ in benzene and 668 $cm^{-1}$ in toluene, are close to that in DCM (892 $cm^{-1}$) (Wu et al., 2017) and comparable with those for other moderately strongly coupled systems (Xiao et al., 2013). Of these two solvents, benzene gives the system a smaller $H_{ab}$, showing some quadrupolar effects, instead of dipole effect, whereas in toluene, the IVCT spectrum features lower transition

energy (2,062 $cm^{-1}$), higher intensity (7,760 $M^{-1}cm^{-1}$), and smaller half-height bandwidth (1,845 $cm^{-1}$), indicating the stronger electronic coupling and typical dipole solvation behaviors. Obviously, the differences in mixed valency for the complexes in different solvents are caused by the subtle differences in the host-guest geometry and the magnitude of quadrupole moment between these two solvents. In hexafluorobenzene, there appear in the spectra typical absorption bands for MV $Mo_2$ dimers, $\delta \rightarrow \delta^*$ at 440 nm, MLCT at 585 nm, LMCT at 790 nm, and IVCT at 5,745 $cm^{-1}$, although the absorbances are very weak (Figure S9), different from the charge transfer absorbances for $[\mathbf{thi\text{-}(OS)_2}]^+$ and $[\mathbf{thi\text{-}(SS)_2}]^+$ in the same solvent. Analysis of the IVCT band gives a $H_{ab}$ of 580 $cm^{-1}$, indicating a significant electronic decoupling effect. It is clear that, for $[\mathbf{thi\text{-}(NS)_2}]^+$, the MV property is less affected by the aromatic solvents. As a result, this complex is even more strongly coupled than the other two analogues in the series. Collectively, the quadrupole effects on the mixed-valency and the IVCT spectra of the MV series are fully in accordance with host-guest geometries in the space-filling models. These results demonstrate an MV transition from strongly coupled Class III to weakly coupled Class II. Significantly, the system transition is realized by site-specific, single-molecule interactions, intrinsically different from dipole solvation (Creutz, 1983; Demadis et al., 2001; Chen and Meyer, 1998) and solvent dynamic effect (Rossky and Simon, 1994; Lear et al., 2007).

### Impacts of the Quadrupolar Effects on the ET Rates ($k_{et}$)

According to the transition state theory, the through-bond ET rate for MV compounds is limited by the nuclear vibrational frequency, ca. $5 \times 10^{12}$ $s^{-1}$ (Creutz, 1983; Brunschwig et al., 2002; Brunschwig and Sutin, 1999). In DCM, $[\mathbf{thi\text{-}(OS)_2}]^+$ and $[\mathbf{thi\text{-}(SS)_2}]^+$ exhibit typical Class II-III and Class III spectral features and parameters (Figure 5 and Table 2), respectively, from which ET rates of $5 \times 10^{12}$ $s^{-1}$ are assigned arbitrarily. For those in Class II, the valence electrons are trapped to a varying extent with respect to the vibrational timescale ($10^{-12}$ s, or picoseconds). The thermal ET dynamics can be described adiabatically from the magnitude of $H_{ab}$ under the semi-classical theoretic framework (Creutz, 1983; Demadis et al., 2001; Marcus and Sutin, 1985; Brunschwig and Sutin, 1999; Newton and Sutin, 1984). Combination of the Marcus theory of ET kinetics and Hush optical analysis of EC matrix element allows determination of ET dynamics ($\Delta G^*$) and kinetics ($k_{et}$) at the level of the transition state from Equations 3 and 4.

$$\Delta G^* = \frac{(\lambda - 2H_{ab})^2}{4\lambda} \qquad \text{(Equation 3)}$$

$$k_{et} = A \exp\left(-\frac{\Delta G^*}{k_B T}\right) \qquad \text{(Equation 4)}$$

In Equation 3, the reorganization energy $\lambda = E_{IT} + \Delta G^0$ and for symmetric systems ($\Delta G^0 = 0$), $\lambda = E_{IT}$ (Creutz, 1983; Marcus, 1993; Marcus and Sutin, 1985). In Equation 4, the prefactor $A$ is the product of electronic factor $\kappa$ and electronic frequency $\nu_{el}$ or nuclear frequency $\nu_n$, depending on the magnitudes of $\nu_{el}$ and $\nu_n$ (Brunschwig and Sutin, 1999; Sutin, 1983). For these $Mo_2$ dimers, $A = 5.0 \times 10^{12}$ $s^{-1}$ by applying an averaged nuclear frequency ($\nu_n = 5.0 \times 10^{12}$ $s^{-1}$) because $\nu_{el} >> 2\nu_n$ and the electronic factor $\kappa \approx 1$ (Yu et al., 2016; Xiao et al., 2014; Chisholm and Patmore, 2007). Calculations yield the ET rate constants ($k_{et}$) in the range of $10^{10}$–$10^{12}$ $s^{-1}$ for the complex series in different solvents (Table 2). For $[\mathbf{thi\text{-}(OS)_2}]^+$ and $[\mathbf{thi\text{-}(SS)_2}]^+$ in $C_6F_6$, the strong quadrupole-quadrupole interactions preclude optical determination of $k_{et}$. In benzene and toluene, the $k_{et}$ values are lowered by 1–2 orders of magnitude. For $[\mathbf{thi\text{-}(NS)_2}]^+$, similar ET rates ($\sim 10^{12}$ $s^{-1}$) are found in benzene, toluene, and DCM, as expected from the similar spectral features, whereas in hexafluorobenzene, the $k_{et}$ is lowered to $6.0 \times 10^{10}$ $s^{-1}$ (Table 2).

## DISCUSSION

This study shows that perturbation of the bridge by interaction with an associated guest molecule is able to shift an MV system from the delocalized to the localized regime and gate the D-A ET by directly intervening with the bridge $\pi$ orbital that serves as the charge transfer platform. Therefore, the quadrupolar effects on EC and ET are best described as *solvent-mediated superexchange decoupling*, in contrast to the reported *solvent-mediated superexchange coupling* (Han and Zimmt, 1998; Read et al., 1999; Napper et al., 2002; Paddon-Row, 2003; Kumar et al., 1996). The contrary behaviors of aromatic solvents are due to the different bonding characters of the bridge in the D-B-A systems. Unlike the present complexes, in the U-shaped organic D-B-A molecules, the bridges are built by covalent $\sigma$ bonds, which do not function well for through-bond superexchange; thus, inserting an aromatic molecule improves the donor-acceptor electronic communication. In this study, the $2H_{ab}/\lambda$ values for $[\mathbf{thi\text{-}(OS)_2}]^+$ and $[\mathbf{thi\text{-}(SS)_2}]^+$ decrease from 1.0

to ~0.2 (Table 2) with changing the solvent from DCM to benzene (or toluene), showing the efficient mediation of quadrupolar effects on the EC (Brunschwig et al., 2002). In chemical D-B-A systems, a general strategy to control EC and ET is to modify the geometric and electronic properties of the bridge. Remarkably, here, dramatic electronic decoupling occurs in mixed-valent state in the quadrupole solvents, whereas the $\{[Mo_2]\text{-}C_4H_2S\text{-}[Mo_2]\}^+$ structure remains intact. This means that taking advantage of geometric and electronic complementarities between the host and guest molecules, one can tune the electronic coupling through non-covalent interactions, which is controllable and reversible.

Moreover, calculations show that inclusion of an aromatic molecule increases the low-lying $\pi^*$ orbital energy and stabilizes the ground state by decreasing the high-lying $\pi$ orbital energy. Thus, we can estimate the stabilizing energy ($-\Delta G^\circ$) or free energy of association ($\Delta G^\circ$) from the decrease of the occupied $\pi$ orbital energy, which equals approximately the change of HOMO-LUMO energy gap or $\Delta\Delta E_{H\text{-}L}$ in the aromatic solvents relative to the $\Delta E_{H\text{-}L}$ in DCM. The calculated $\Delta\Delta E_{H\text{-}L}$ data are compared with the experimental results ($\Delta E_{ML}$), as shown in Table 1. In hexafluorobenzene, [**thi-(OS)$_2$**] and [**thi-(SS)$_2$**] present the $\Delta\Delta E_{H\text{-}L}$ ($\approx -\Delta G^\circ$) values of 4.1 and 5.5 kcal mol$^{-1}$, respectively, close to the calculated stabilizing energy of 3.7 kcal mol$^{-1}$ for the $C_6H_6\text{-}C_6F_6$ adduct (West et al., 1997). This stabilization energy, gained by $C_6F_6\text{-}C_4H_2S$ quadrupolar interaction, is reasonably smaller than the association energy (7.1 kcal mol$^{-1}$) for $C_6F_6$ parallel stacked on the top of Zn porphyrin with a short separation (2.93 Å) (Morisue et al., 2017). In benzene (toluene), the $\Delta\Delta E_{H\text{-}L}$ values fall in the range of 2.1–3.0 kcal mol$^{-1}$ (Table 1), in excellent agreement with the calculated stabilizing energy (Hobza et al., 1996) of 2.3 kcal mol$^{-1}$ and the association energy (Tsuzuki and Uchimaru, 2006) of 2.46 kcal mol$^{-1}$ for the T-shaped benzene dimers.

Shown in Figures 6A–6C are the plots of $\Delta\Delta E_{H\text{-}L}$ against the effective quadrupole moments $\langle Q\rangle$ (Reynolds et al., 1996), in comparison with the spectroscopic data, $\Delta E_{ML}$ versus $\langle Q\rangle$. For [**thi-(OS)$_2$**] and [**thi-(SS)$_2$**], a good linear relationship between $\Delta\Delta E_{H\text{-}L}$ and $\langle Q\rangle$ is found. For [**thi-(OS)$_2$**] (Figure 6B), the linear plot of $\Delta\Delta E_{H\text{-}L}$ versus $\langle Q\rangle$ has a larger slope than that for [**thi-(SS)$_2$**] (Figure 6C), indicating the larger decoupling effects, which is in contrast to its larger coupling constants $H_{ab}$. The stronger quadrupolar effects for [**thi-(OS)$_2$**] from calculations can be rationalized by the electronegative O chelating atoms of the bridging ligand, which then enhances the host-guest electrostatic interactions, as indicated by the larger density contribution of the guest molecule to the LUMO (Figures 4 and S7). On the other hand, the relatively small decoupling effects (relatively large $H_{ab}$) in solution is likely due to the V-shaped cleft of the molecular structure (Figure 3B) that prevents the guest molecule getting close to the $C_4H_2S$ bridge as much as in [**thi-(SS)$_2$**]. Remarkably, linear correlations of $\Delta E_{ML}$ versus $\langle Q\rangle$ are also obtained in both systems (Figures 6B and 6C and Table 1), which are nearly parallel to the theoretical results. The deviations between the experimental and theoretical results can be rationalized by the dipole solvation and molecular dynamics in solution. In benzene and toluene, the changes of the MLCT energies or $\Delta E_{ML}$, ca. 0.7–1.6 kcal mol$^{-1}$ (Table 1), which may be considered to be the experimental values of stabilizing energy ($-\Delta G^\circ$) of the supramolecular systems, are in excellent agreement with the free energies ($\Delta G^\circ$ = −0.6 to −1.3 kcal mol$^{-1}$) contributed by aromatic pairs in protein (Burley and Petsko, 1985). In contrast to [**thi-(OS)$_2$**] and [**thi-(SS)$_2$**], [**thi-(NS)$_2$**] does not exhibit the linear relationship between the $\Delta\Delta E_{H\text{-}L}$ (or $\Delta E_{ML}$) and the solvent $\langle Q\rangle$ values (Figure 6A and Table 1). These results are understandable from the simultaneous presence of weak site-specific quadrupole interactions and significant dipole solvation, as expected from the space-filling models and the calculated results. Therefore, for this $Mo_2$ D-B-A system, the increase of the HOMO-LUMO energy gap is a good estimate of the stabilizing energy of including an aromatic molecule through quadrupole-quadrupole interaction, which provides a vital interpretation on the supramolecular complementarity in constitution, electronic state, and energetics.

The quadrupole-quadrupole interactions in these supramolecular complex systems are visualized by the electrostatic potential maps generated from DFT calculations on the simplified models. The electrostatic potential maps (Figure 6D) show that the free benzene (toluene) and hexafluorobenzene molecules display opposite charge distributions surrounding the $C_6$ rings, as depicted in Figure 1. Of the three complex models, the electrostatic potentials vary in the order of [**thi-(NS)$_2$**]′ > [**thi-(SS)$_2$**]′ > [**thi-(OS)$_2$**]′. This order is consistent with that of the electrochemical potentials $E_{1/2}(1)$ of the complexes in DCM, that is, 0.41 V ([**thi-(NS)$_2$**]), 0.42 V([**thi-(SS)$_2$**]), and 0.48 V ([**thi-(OS)$_2$**]) (versus Ag/AgCl) (Wu et al., 2017). The relatively low electrostatic potential for [**thi-(OS)$_2$**]′ is likely due to the presence of more electronegative O chelating atoms of the bridging ligand. For the three supramolecular entities, as shown in Figure 6E, the electrostatic potential surfaces for the guest molecules vary substantially, but not apparently for the host complexes, because the charge redistribution is

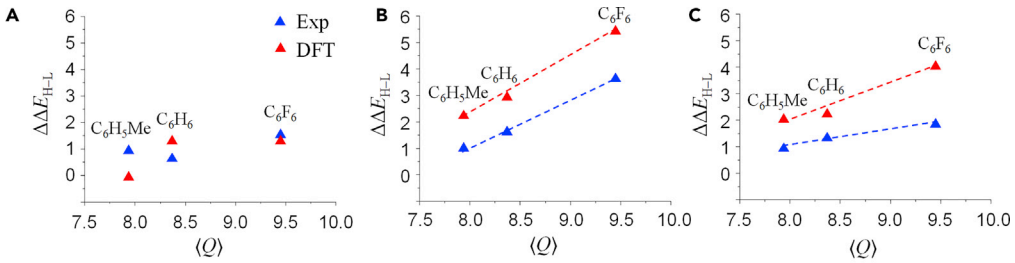
A
B
C
Exp
DFT
$C_6H_5Me$
$C_6H_6$
$C_6F_6$
$\Delta\Delta E_{H-L}$
$\langle Q \rangle$

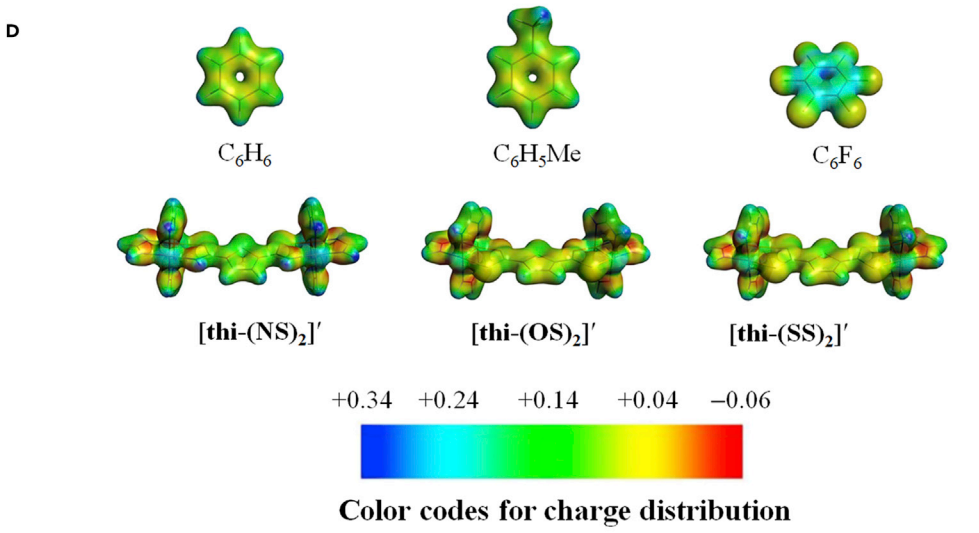
D
$C_6H_6$
$C_6H_5Me$
$C_6F_6$
[thi-$(NS)_2$]′
[thi-$(OS)_2$]′
[thi-$(SS)_2$]′
+0.34 +0.24 +0.14 +0.04 −0.06
Color codes for charge distribution

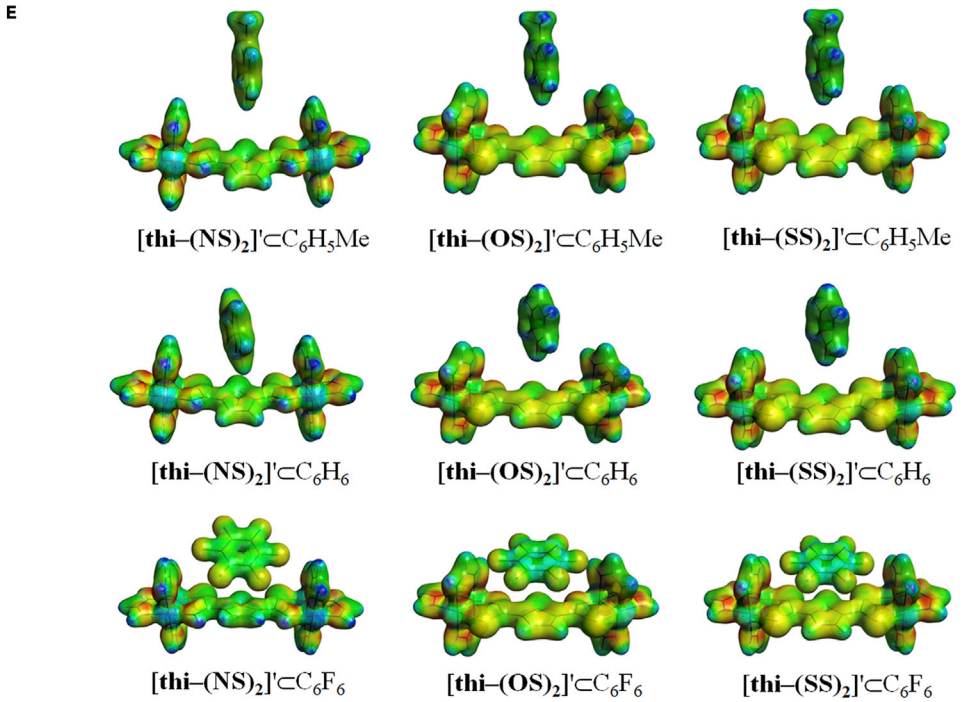
E
[thi–$(NS)_2$]′⊂$C_6H_5Me$
[thi–$(OS)_2$]′⊂$C_6H_5Me$
[thi–$(SS)_2$]′⊂$C_6H_5Me$
[thi–$(NS)_2$]′⊂$C_6H_6$
[thi–$(OS)_2$]′⊂$C_6H_6$
[thi–$(SS)_2$]′⊂$C_6H_6$
[thi–$(NS)_2$]′⊂$C_6F_6$
[thi–$(OS)_2$]′⊂$C_6F_6$
[thi–$(SS)_2$]′⊂$C_6F_6$

**Figure 6. Correlations of $\Delta\Delta E_{H\text{-}L}$ and $\Delta E_{ML}$ with Quadrupole Moments of the Aromatic Solvents in Use and Electrostatic Potential Maps of the Free Aromatic Solvent and Complex Molecules and the Supramolecular Entities**

(A–C) Plots of changes of the HOMO−LUMO energy gaps ($\Delta\Delta E_{H\text{-}L}$) of complex models in aromatic solvents, relative to that in DCM, against the effective quadrupole moments $\langle Q \rangle$ of the solvent molecules (SM), along with the experimental data $\Delta E_{ML}$ versus $\langle Q \rangle$, showing the quadrupole effects for supramolecular systems [**thi-(NS)$_2$**]⊂SM (A), [**thi-(OS)$_2$**]⊂SM (B), and [**thi-(SS)$_2$**]⊂SM (C) (SM = $C_6H_5Me$, $C_6H_6$ and $C_6F_6$).

(D and E) The DFT calculated electrostatic potential surface maps for the complexes and free aromatic solvent molecules (D) and the complex systems with a solvent molecule encapsulated (E). For both of the molecular and supramolecular systems, the electrostatic potential maps refer to the same color codes as shown.

averaged or "diluted" by the large number of atoms on the complex molecule. Importantly, in the systems of [**thi-(OS)$_2$**]′ and [**thi-(SS)$_2$**]′ (Figure 6E), the overall electrostatic potentials for the included $C_6H_5Me$ and $C_6H_6$ molecules increase, in comparison with the free solvent molecules (Figure 6D); in contrast, the included $C_6F_6$ molecule exhibits lower electrostatic potentials compared with free $C_6F_6$. Therefore, the electrostatic potential maps of the guest molecules demonstrate that benzene and toluene molecules, as electron donors, contribute $\pi$ electron density to the host molecule through quadrupole-quadrupole interaction, whereas the hexafluorobenzene molecule is the electron acceptor because of the electron deficiency of the ring center (Figure 6D). The electrostatic potential maps for the supramolecular systems are in accordance with the IVCT spectra of the complexes in the aromatic solvents. For [**thi-(NS)$_2$**], the variation of electrostatic potential maps is less pronounced; similarly, the spectral changes of the MV complex in the aromatic solvents are minor, except for the case of hexafluorobenzene.

On the basis of the experimental observations and the computational results, the perturbation of the guest molecule on the ET dynamics and mechanism can be described by Figure 7. Pictorially, in the supramolecular ET systems, typically, for [**thi-(OS)$_2$**]$^+$ and [**thi-(SS)$_2$**]$^+$, the guest molecule $C_6H_6$ or $C_6H_5Me$ vertically standing in the middle of the D-B-A molecule builds a "wall" that blocks the electrons transferring from the donor to the acceptor (Figure 7B). Electronically, the intervening molecule donates $\pi$ electron density to the anti-bonding bridge $\pi^*$ orbital, diminishing the d($\delta$)-p($\pi$) orbital interaction between the $Mo_2$ centers and the bridge. In the two-state model, the ET energetics are characterized by the higher reorganization energy ($\lambda$) and activation energy ($\Delta G^*$). The single, Gaussian-shaped IVCT band in the spectra (Figure 5) implies that the system retains its original ET reaction coordinate, with increased $\lambda$ and decreased $H_{ab}$. Correspondingly, the single-well potential energy surfaces (PES) for ET (Figure 7A) are altered to a double-well PES diagram (Figure 7B). The ET process is dominated by the through-bond superexchange mechanism (McConnell, 1961), as evidenced by the presence of MLCT and LMCT in the spectra for the MV complexes (Figures S10 and S11) (Creutz et al., 1994). However, for systems in hexafluorobenzene, there is no characteristic IVCT band observed. The broad, weak absorbances in the near-mid-IR region dictate that the system undergoes a different ET process via a distinct mechanism. In this scenario, considering that the $C_6$ ring center is electron deficient, we propose that the $C_6F_6$ molecule lying on the top of the $C_4H_2S$ group plays a role of electron relay for the D-A ET, which is schematically represented in Figure 7C. In the ET course, the $C_6F_6$ molecule serves as an acceptor with respect to the $Mo_2$ donor, but a donor for the $Mo_2$ acceptor for completion of the two electron hopping steps. This hypothesis is further supported by the absence of an LMCT band in the spectra of the MV complexes (Figures S10 and S11), indicating that the electron-hole superexchange pathway is not in operation (Liu et al., 2013; Creutz et al., 1994). Accordingly, the two-state model for the ET reaction is constructed with two asymmetrical potential energy surfaces crossing over the transition state of the reaction, as described in Figure 7C. Continuous electron hopping from the $Mo_2$ donor to acceptor generates the broad, featureless, weak charge transfer absorptions as observed (Figures 5B and 5C). As a result of intervening of the $C_6F_6$ molecule, the ET system is transformed from the adiabatic to the non-adiabatic regimes. However, in [**thi-(NS)$_2$**]$^+$⊂$C_6F_6$, in which the $C_6F_6$ molecule stays further from the $C_4H_2S$ bridge, the perturbation on the ET reaction is not as strong as in [**thi-(OS)$_2$**]$^+$⊂$C_6F_6$ and [**thi-(SS)$_2$**]$^+$⊂$C_6F_6$, as evidenced by the MLCT, LMCT, and IVCT bands in the spectra (Creutz et al., 1994), although the ET rate is significantly reduced (Table 2). Therefore, in this system, electron transfer proceeds via the through-bridge superexchange pathway as shown in Figure 7D.

Collectively, three MV [$Mo_2$]-$C_4H_2S$-[$Mo_2$] complexes in DCM belong to three different mixed-valent regimes, Classes II, II-III, and III in the Robin-Day's classification, by changing the chelating atoms from N to O and S. Surprisingly, in the aromatic solvents, such as, benzene, toluene, and hexafluorobenzene, the IVCT characteristics are significantly altered; the electronic coupling matrix elements ($H_{ab}$) and electron

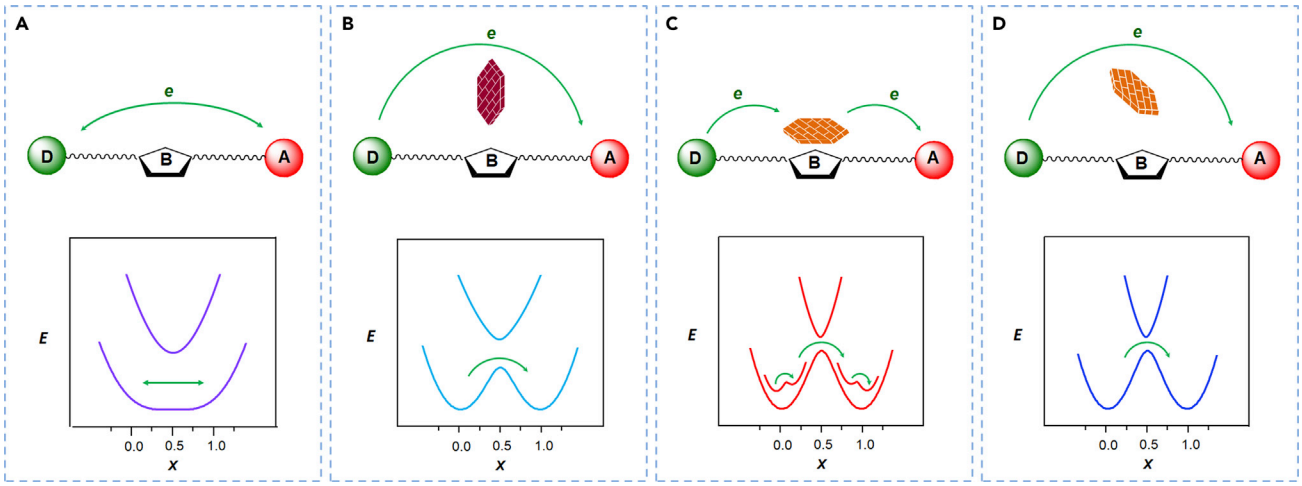


**Figure 7. Schematic Illustration of Quadrupole Effects on Thermal Electron Transfer in the Mixed-Valence $Mo_2$ Dimers**

(A–D) Donor-bridge-acceptor models (top) and the corresponding ET potential energy surface diagrams (bottom) for $[\textbf{thi-(OS)}_2]^+$ and $[\textbf{thi-(SS)}_2]^+$ in DCM (A), benzene (B), and hexafluorobenzene (C) and for $[\textbf{thi-(NS)}_2]^+$ in hexafluorobenzene (D).

transfer rate constants ($k_{et}$), determined by optical analysis under the Marcus-Hush theory, are dramatically reduced, in contrast to the predications from the dielectric continuum model. Space-filling models developed by DFT calculations show that an aromatic molecule is encapsulated in the cleft of the D-B-A molecule, contacting with the $C_4H_2S$ ring in T-shaped (for benzene and toluene) or face-to-face (for hexafluorobenzene) geometries with varying distances (4.0–6.9 Å). Remarkably, it is found that, in the aromatic solvents, the magnitudes of $H_{ab}$ and $k_{et}$ are correlated to the strength of quadrupole-quadrupole interactions between the guest molecule and the $C_4H_2S$ bridge. Theoretical results reveal that the quadrupole effect evokes a charge redistribution of the bridging ligand and increases the HOMO-LUMO gap, consequently gating the electron transfer from one $Mo_2$ center to the other. From the increase of the low-lying $\pi^*$ orbital energy the stabilizing energies for the supramolecular systems are estimated to be 2.2–5.5 kcal $mol^{-1}$. Evidently, intervening of the guest molecule to the bridge modifies the electronic structure and alters the ET pathway; thus, the D-B-A system undergoes a chemical transformation without bond breakage and formation. Therefore, this work, with the rare examples, demonstrates that a supramolecular system is unified underlying the characteristics of the assembled molecules through constitutional, electronic, and energetic complementarities. With the molecular signature on "the chemistry beyond the molecule" provided in this study, it is substantiated that the general principles developed in molecular chemistry are universal, which govern supramolecular systems as well.

## Limitations of the Study

In this study, the stabilization energies of the supramolecular systems through quadrupole-quadrupole interaction were estimated based on the measured MLCT energies or calculated HOMO-LUMO gaps. No strict theoretic calculations of the potential energy for the system were performed, although reasonable results were obtained in comparison with the literature data. As the investigation goes deep, the issues of energetic complementary of the supramolecular system can be further addressed using well-developed theoretic methods. In the $Mo_2$-$Mo_2$ mixed-valance system with a saturated bridge, enhancement of electronic coupling through solute-solvent interactions, as seen in the organic U-shaped systems in photoinduced ET, was not observed.

## METHODS

All methods can be found in the accompanying Transparent Methods supplemental file.

## DATA AND CODE AVAILABILITY

The X-ray crystallographic data ($[\textbf{thi-(NS)}_2]$, $[\textbf{thi-(OS)}_2]$ and $[\textbf{thi-(SS)}_2]$) reported in this study have been deposited at the Cambridge Crystallographic Data Centre (CCDC), under deposition number CCDC 1935628-1935630.

## SUPPLEMENTAL INFORMATION

Supplemental Information can be found online at https://doi.org/10.1016/j.isci.2019.11.020.

## ACKNOWLEDGMENTS

We acknowledge the primary financial support from the National Natural Science Foundation of China (21371074, 90922010), Natural Science Foundation of Guangdong Province (2018A030313894), Jinan University, and the Fundamental Research Funds for the Central Universities of China.

## AUTHOR CONTRIBUTIONS

C.Y.L. conceived the research objective and designed the experiments and worked on the manuscript. S.M. performed DFT theoretical calculations and data analysis and assisted in the writing of the paper. L.C. carried out the major experimental work and data analysis. X.C., J.Z., Y.Q., G.Y.W., and Y.Y.W. were involved in compound syntheses and electrochemical and spectroscopic measurements. M.M. completed the data collection and analysis of the X-ray crystal structures. G.Y.Z., Y.N.T., and T.C. participated in discussion of the results.

## DECLARATION OF INTERESTS

The authors declare no competing interests.

Received: July 19, 2019
Revised: November 6, 2019
Accepted: November 9, 2019
Published: December 20, 2019

## REFERENCES

Balzani, V. (2001). Electron transfer in chemistry (Wiley-VCH). https://doi.org/10.1002/9783527618248.

Brunschwig, B.S., and Sutin, N. (1999). Energy surfaces, reorganization energies, and coupling elements in electron transfer. Coord. Chem. Rev. *187*, 233–254.

Brunschwig, B.S., Creutz, C., and Sutin, N. (2002). Optical transitions of symmetrical mixed-valence systems in the Class II–III transition regime. Chem. Soc. Rev. *31*, 168–184.

Burley, S.K., and Petsko, G.A. (1985). Aromatic-aromatic interaction—a mechanism of protein-structure stabilization. Science *229*, 23–28.

Calladine, C.R., Drew, H.R., Luisi, B., and Travers, A. (2004). Understanding DNA: The Molecule and How it Works, Third Edition (Academic Press).

Chakrabarti, S., Parker, M.F.L., Morgan, C.W., Schafmeister, C.E., and Waldeck, D.H. (2009). Experimental evidence for water mediated electron transfer through bis-amino acid donor-bridge-acceptor oligomers. J. Am. Chem. Soc. *131*, 2044–2045.

Chen, P., and Meyer, T.J. (1998). Medium effects on charge transfer in metal complexes. Chem. Rev. *98*, 1439–1478.

Chen, X., Tao, Y., Li, J., Dai, H., Sun, W., Huang, X., and Wei, Z. (2012). Aromatic residues regulating electron relay ability of S-containing amino acids by formations of S∴π multicenter three-electron bonds in proteins. J. Phys. Chem. C *116*, 19682–19688.

Chen, H.W., Mallick, S., Zou, S.F., Meng, M., and Liu, C.Y. (2018). Mapping bridge conformational effects on electronic coupling in $Mo_2$—$Mo_2$ mixed-valence systems. Inorg. Chem. *57*, 7455–7467.

Chisholm, M.H., and Patmore, N.J. (2007). Studies of electronic coupling and mixed valency in Metal—Metal quadruply bonded complexes linked by dicarboxylate and closely related ligands. Acc. Chem. Res. *40*, 19–27.

Chisholm, M.H., Feil, F., Hadad, C.M., and Patmore, N.J. (2005). Electronically coupled MM quadruply-bonded complexes (M= Mo or W) employing functionalized terephthalate bridges: toward molecular rheostats and switches. J. Am. Chem. Soc. *127*, 18150–18158.

Concepcion, J.J., Dattelbaum, D.M., Meyer, T.J., and Rocha, R.C. (2007). Probing the localized-to-delocalized transition. Philos. Trans. A Math. Phys. Eng. Sci. *366*, 163–175.

Cotton, F.A., Donahue, J.P., Murillo, C.A., and Pérez, L.M. (2003). Polyunsaturated dicarboxylate tethers connecting dimolybdenum redox and chromophoric centers: absorption spectra and electronic structures. J. Am. Chem. Soc. *125*, 5486–5492.

Cotton, F.A., Murillo, C.A., and Walton, R.A. (2005). Multiple Bonds between Metal Atoms, Third Edition (Springer).

Cotton, F.A., Li, Z., Liu, C.Y., and Murillo, C.A. (2007). Modulating electronic coupling using O- and S-donor linkers. Inorg. Chem. *46*, 7840–7847.

Creutz, C. (1983). Mixed valence complexes of d5-d6 metal centers. Prog. Inorg. Chem. *30*, 1–73.

Creutz, C., Newton, M.D., and Sutin, N. (1994). Metal—ligand and metal—metal coupling elements. J. Photochem. Photobiol. A *82*, 47–59.

Crutchley, R.J. (1994). Intervalence charge transfer and electron exchange studies of dinuclear ruthenium complexes. Adv. Inorg. Chem. *41*, 273–325.

Demadis, K.D., Hartshorn, C.M., and Meyer, T.J. (2001). The localized-to-delocalized transition in mixed-valence chemistry. Chem. Rev. *101*, 2655–2686.

Dougherty, D.A. (1996). Cation-π interactions in chemistry and biology: a new view of benzene, Phe, Tyr, and Trp. Science *271*, 163–168.

Finzel, B.C., Baldwin, E.T., Bryant, G.L., Hess, G.F., Jr., Wilks, J.W., Trepod, C.M., Mott, J.E., Marshall, V.P., Petzold, G.L., Poorman, R.A., et al. (1998). Structural characterizations of nonpeptidic thiadiazole inhibitors of matrix metalloproteinases reveal the basis for stromelysin selectivity. Protein Sci. *7*, 2118–2126.

Ford, P.C., Rudd, D.F.P., Gaunder, R., and Taube, H. (1968). Synthesis and properties of pentaamminepyridineruthenium(II) and related pentaammineruthenium complexes of aromatic nitrogen heterocycles. J. Am. Chem. Soc. *90*, 1187–1194.

Gao, H., Mallick, S., Cao, L., Meng, M., Cheng, T., Chen, H.W., and Liu, C.Y. (2019). Electronic coupling and electron transfer between two $Mo_2$ Units through *meta*- and *para*-phenylene bridges. Chem. Eur. J. *25*, 3930–3938.

Glover, S.D., Goeltz, J.C., Lear, B.J., and Kubiak, C.P. (2010). Inter- or intramolecular electron

transfer between triruthenium clusters: we'll cross that bridge when we come to it. Coord. Chem. Rev. *254*, 331–345.

Graff, B., Lamont, D.N., Parker, M.F.L., Bloom, B.P., Schafmeister, C.E., and Waldeck, D.H. (2016). Through-solvent tunneling in donor–bridge–acceptor molecules containing a molecular cleft. J. Phys. Chem. A *120*, 6004–6013.

Han, H., and Zimmt, M.B. (1998). Solvent-mediated electron transfer: correlation between coupling magnitude and solvent vertical electron affinity. J. Am. Chem. Soc. *120*, 8001–8002.

Hobza, P., Selzle, H.L., and Schlag, E.W. (1996). Potential energy surface for the benzene dimer. Results of ab initio CCSD(T) calculations show two nearly isoenergetic structures: T-shaped and parallel-displaced. J. Phys. Chem. *100*, 18790–18794.

Hunter, C.A., Lawson, K.R., Perkins, J., and Urch, C. (2001). Aromatic interactions. J. Chem. Soc. Perkin Trans. *2*, 651–669.

Hupp, J.T., Neyhart, G.A., and Meyer, T.J. (1986). Solvent control of oxidation state distribution and electronic delocalization in an osmium-ruthenium, mixed-metal dimer. J. Am. Chem. Soc. *108*, 5349–5350.

Hush, N.S. (1967). Intervalence-transfer absorption. Part 2. Theoretical considerations and spectroscopic data. Prog. Inorg. Chem. *8*, 391–444.

Hush, N.S. (1968). Homogeneous and heterogeneous optical and thermal electron transfer. Electrctrochim. Acta *13*, 1005–1023.

Kang, M.T., Meng, M., Tan, Y.N., Cheng, T., and Liu, C.Y. (2016). Tuning the electronic coupling and electron transfer in $Mo_2$ donor–acceptor systems by variation of the bridge conformation. Chem. Eur. J. *22*, 3115–3126.

Kubiak, C.P. (2013). Inorganic electron transfer: sharpening a fuzzy border in mixed valency and extending mixed valency across supramolecular systems. Inorg. Chem. *52*, 5663–5676.

Kumar, K., Lin, Z., Waldeck, D.H., and Zimmt, M.B. (1996). Electronic coupling in C-Clamp-Shaped Molecules: solvent-mediated superexchange pathways. J. Am. Chem. Soc. *118*, 243–244.

Lear, B.J., Glover, S.D., Salsman, J.C., Londergan, C.H., and Kubiak, C.P. (2007). Solvent dynamical control of ultrafast ground state electron transfer: implications for Class II-III mixed valency. J. Am. Chem. Soc. *129*, 12772–12779.

Lee, E.C., Kim, D., Jurečka, P., Tarakeshwar, P., Hobza, P., and Kim, K.S. (2007). Understanding of assembly phenomena by aromatic-aromatic interactions: benzene dimer and the substituted systems. J. Phys. Chem. A *111*, 3446–3457.

Lehn, J.-M. (2002). Toward self-organization and complex matter. Science *295*, 2400–2403.

Lehn, J.-M. (2007). From supramolecular chemistry towards constitutional dynamic chemistry and adaptive chemistry. Chem. Soc. Rev. *36*, 151–160.

Lin, J., Balabin, I.A., and Beratan, D.N. (2005). The nature of aqueous tunneling pathways between electron-transfer proteins. Science *310*, 1311–1313.

Liu, C.Y., Xiao, X., Meng, M., Zhang, Y., and Han, M.J. (2013). Spectroscopic study of δ electron transfer between two covalently bonded dimolybdenum units via a conjugated bridge: adequate complex models to test the existing theories for electronic coupling. J. Phys. Chem. C *117*, 19859–19865.

Marcus, R.A. (1956). On the theory of oxidation-reduction reactions involving electron transfer. J. Chem. Phys. *24*, 966–978.

Marcus, R.A. (1964). Chemical and electrochemical electron-transfer theory. Annu. Rev. Phys. Chem. *15*, 155–196.

Marcus, R.A. (1993). Electron transfer reactions in chemistry: theory and experiment (Nobel lecture). Angew. Chem. Int. Ed. *32*, 1111–1121.

Marcus, R.A., and Sutin, N. (1985). Electron transfers in chemistry and biology. Biochem. Biophys. Acta *811*, 265–322.

McConnell, H.M. (1961). Intramolecular charge transfer in aromatic free radicals. J. Chem. Phys. *35*, 508–515.

Meyer, E.A., Castellano, R.K., and Diederich, F. (2003). Interactions with aromatic rings in chemical and biological recognition. Angew. Chem. Int. Ed. *42*, 1210–1250.

Migliore, A., Polizzi, N.F., Therien, M.J., and Beratan, D.N. (2014). Biochemistry and theory of proton-coupled electron transfer. Chem. Rev. *114*, 3381–3465.

Miyashita, O., Okamura, M.Y., and Onuchic, J.N. (2005). Interprotein electron transfer from cytochrome $c_2$ to photosynthetic reaction center: tunneling across an aqueous interface. Proc. Natl. Acad. Sci. U S A *102*, 3558–3563.

Morisue, M., Ueno, I., Shimizu, M., Yumura, T., and Ikeda, N. (2017). Porphyrins sheathed in quadrupolar solvation spheres of hexafluorobenzene: solvation-induced fluorescence enhancement and conformational confinement. J. Phys. Chem. C *121*, 19407–19413.

Napper, A.M., Head, N.J., Oliver, A.M., Shephard, M.J., Paddon-Row, M.N., Read, I., and Waldeck, D.H. (2002). Use of U-shaped donor-bridge-acceptor molecules to study electron tunneling through nonbonded contacts. J. Am. Chem. Soc. *124*, 10171–10181.

Newton, M.D. (1991). Quantum chemical probes of electron-transfer kinetics: the nature of donor-acceptor interactions. Chem. Rev. *91*, 767–792.

Newton, M.D., and Sutin, N. (1984). Electron transfer reactions in condensed phases. Ann. Rev. Phys. Chem. *35*, 437–480.

Neyhart, G.A., Timpson, C.J., Bates, W.D., and Meyer, T.J. (1996). Solvent-induced electron transfer and electronic delocalization in mixed-valence complexes. Spectral properties. J. Am. Chem. Soc. *118*, 3730–3737.

Nishio, M. (2004). CH/π hydrogen bonds in crystals. CrystEngComm *6*, 130–158.

Paddon-Row, M.N. (2003). Superexchange-mediated charge separation and charge recombination in covalently linked donor-bridge-acceptor systems. Aust. J. Chem. *56*, 729–748.

Ponzini, F., Zagha, R., Hardcastle, K., and Siegel, J.S. (2000). Phenyl/pentafluorophenyl interactions and the generation of ordered mixed crystals: sym-triphenethynylbenzene and sym-Tris(perfluorophenethynyl)benzene. Angew. Chem. Int. Ed. *39*, 2323–2325.

Read, I., Napper, A., Kaplan, R., Zimmt, M., and Waldeck, D.H. (1999). Solvent-mediated electronic coupling: the role of solvent placement. J. Am. Chem. Soc. *121*, 10976–10986.

Reynolds, L., Gardecki, J.A., Frankland, S.J.V., Horng, M.L., and Maroncelli, M. (1996). Dipole solvation in nondipolar solvents: experimental studies of reorganization energies and solvation dynamics. J. Phys. Chem. *100*, 10337–10354.

Robin, M.B., and Day, P. (1967). Mixed valence chemistry - a study and classification. Adv. Inorg. Chem. Radiochem. *9*, 247–422.

Rossky, P.J., and Simon, J.D. (1994). Dynamics of chemical processes in polar solvents. Nature *370*, 263–269.

Shih, C., Museth, A.K., Abrahamsson, M., Blanco-Rodriguez, A.M., Di Bilio, A.J., Sudhamsu, J., Crane, B.R., Ronayne, K.L., Towrie, M., et al. (2008). Tryptophan-accelerated electron flow through proteins. Science *320*, 1760–1762.

Shu, Y., Lei, H., Tan, Y.N., Meng, M., Zhang, X.C., and Liu, C.Y. (2014). Tuning the electronic coupling in $Mo_2$–$Mo_2$ systems by variation of the coordinating atoms of the bridging ligands. Dalton Trans. *43*, 14756–14765.

Singh, N.J., Min, S.K., Kim, D.Y., and Kim, K.S. (2009). Comprehensive energy analysis for various types of π-interaction. J. Chem. Theory Comput. *5*, 515–529.

Steed, J.W., and Atwood, J.L. (2009). Supramolecular Chemistry, Second Edition (John Wiley & Sons, Ltd).

Sutin, N. (1983). Theory of electron transfer reactions: insights and hind sights. Prog. Inorg. Chem. *30*, 441–444.

Tan, Y.N., Cheng, T., Meng, M., Zhang, Y.Y., Liu, C.Y., Sun, M.F., Zhang, Y., and Low, P.J. (2017). Optical behaviors and electronic properties of $Mo_2$–$Mo_2$ mixed-valence complexes within or beyond the Class III regime: testing the limits of the two-state model. J. Phys. Chem. C *121*, 27860–27873.

Tatko, C.D., and Waters, M.L. (2002). Selective aromatic interactions in β-hairpin peptides. J. Am. Chem. Soc. *124*, 9372–9373.

Thomas, A., Meurisse, R., and Brasseur, R. (2002a). Aromatic side-chain interactions in proteins. II. Near- and far-sequence Phe-X pairs. Proteins *48*, 635–644.

Thomas, A., Meurisse, R., Charloteaux, B., and Brasseur, R. (2002b). Aromatic side-chain interactions in proteins. I. Main structural features. Proteins *48*, 628–634.

Tsuzuki, S., and Uchimaru, T. (2006). Magnitude and physical origin of intermolecular interactions of aromatic molecules: recent progress of computational studies. Curr. Org. Chem. *10*, 745–762.

Waters, M.L. (2002). Aromatic interactions in model systems. Curr. Opin. Chem. Biol. *6*, 736–741.

West, A.P., Jr., Mecozzi, S., and Dougherty, D.A. (1997). Theoretical studies of the supramolecular synthon benzene-hexafluorobenzene. J. Phys. Org. Chem. *10*, 347–350.

Williams, J.H. (2002). The molecular electric quadrupole moment and solid-state architecture. Acc. Chem. Res. *26*, 593–598.

Williams, J.H., Cockcroft, J.K., and Fitch, A.N. (1992). Structure of the lowest temperature phase of the solid benzene-hexafluorobenzene adduct. Angew. Chem. Int. Ed. *31*, 1655–1657.

Wu, Y.Y., Meng, M., Wang, G.Y., Feng, P., and Liu, C.Y. (2017). Optically probing the localized to delocalized transition in $Mo_2$–$Mo_2$ mixed-valence systems. Chem. Commun. (Camb.) *53*, 3030–3033.

Xiao, X., Liu, C.Y., He, Q., Han, M.J., Meng, M., Lei, H., and Lu, X. (2013). Control of the charge distribution and modulation of the Class II–III transition in weakly coupled $Mo_2$–$Mo_2$ systems. Inorg. Chem. *52*, 12624–12633.

Xiao, X., Meng, M., Lei, H., and Liu, C.Y. (2014). Electronic coupling and electron transfer between two dimolybdenum units spaced by a biphenylene group. J. Phys. Chem. C *118*, 8308–8315.

Yu, W.Y., Meng, M., Lei, H., He, X.D., and Liu, C.Y. (2016). Optical determination of electron transfer dynamics and kinetics for asymmetrical $[Mo_2]$–ph–$[Mo_2]$ systems. J. Phys. Chem. C *120*, 12411–12422.

Zeng, J., Hush, N.S., and Reimers, J.R. (1996). Solvent effects on molecular and ionic spectra. 7. Modeling the absorption and electroabsorption spectra of pentaammine-ruthenium(II) pyrazine and its conjugate acid in water. J. Am. Chem. Soc. *118*, 2059–2068.

Zhu, G.Y., Meng, M., Tan, Y.N., Xiao, X., and Liu, C.Y. (2016). Electronic coupling between two covalently bonded dimolybdenum units bridged by a naphthalene group. Inorg. Chem. *55*, 6315–6322.

ISCI, Volume *22*

## Supplemental Information

# Mediation of Electron Transfer by Quadrupolar Interactions: The Constitutional, Electronic, and Energetic Complementarities in Supramolecular Chemistry

**Suman Mallick, Lijiu Cao, Xiaoli Chen, Junpeng Zhou, Yi Qin, Gang Yi Wang, Yi Yang Wu, Miao Meng, Guang Yuan Zhu, Ying Ning Tan, Tao Cheng, and Chun Y. Liu**

## Supplemental Figures

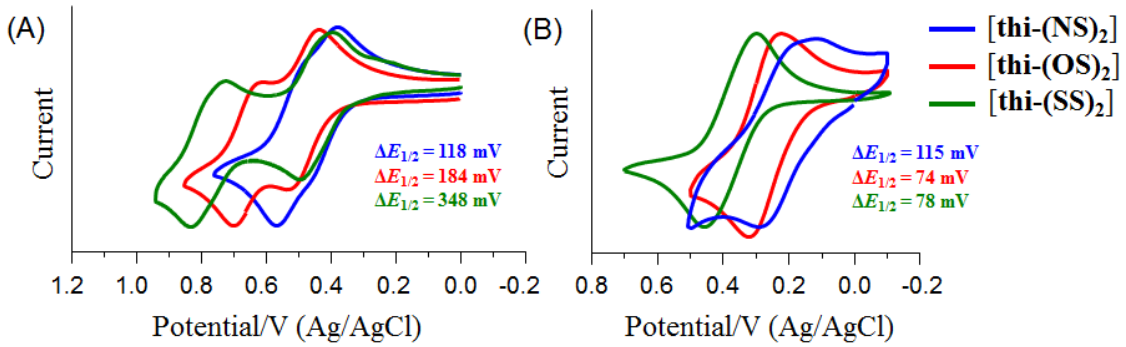


**Figure S1. Cyclic Voltammograms for the complexes, related to Table 2.** Cyclic Voltammograms for [**thi-(NS)$_2$**] (blue), [**thi-(OS)$_2$**] (red), and [**thi-(SS)$_2$**] (green) were measured in (A) dichloromethane and (B) toluene solutions. The redox potential separations ($\Delta E_{1/2}$) were measured from the peak to peak values in the DPVs or from the working curves based on the Richardson–Taube method.

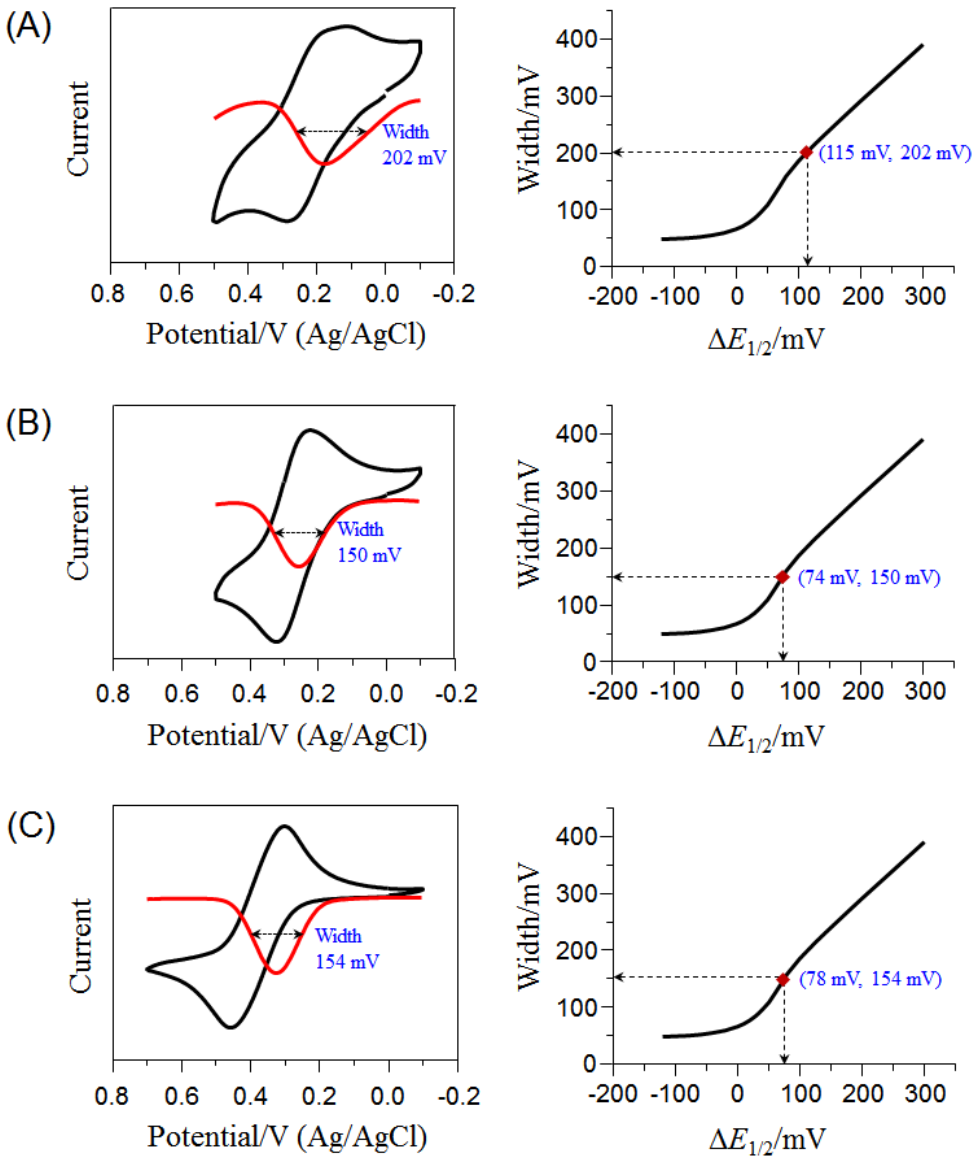


**Figure S2. Estimation of redox potential separations ($\Delta E_{1/2}$) based on Richardson–Taube method, related to Table 2.** Cyclic voltammograms (CVs, black) and differential pulse voltammograms (DPVs, red) are shown for complexes (A) [**thi-(NS)$_2$**], (B) [**thi-OS)$_2$**], and (C) [**thi-(SS)$_2$**] in 0.1 M tetrahexylammonium hexafluorophosphate / toluene solutions. The $\Delta E_{1/2}$ value are estimated from the working curve (width versus $\Delta E_{1/2}$) based on the Richardson–Taube method.

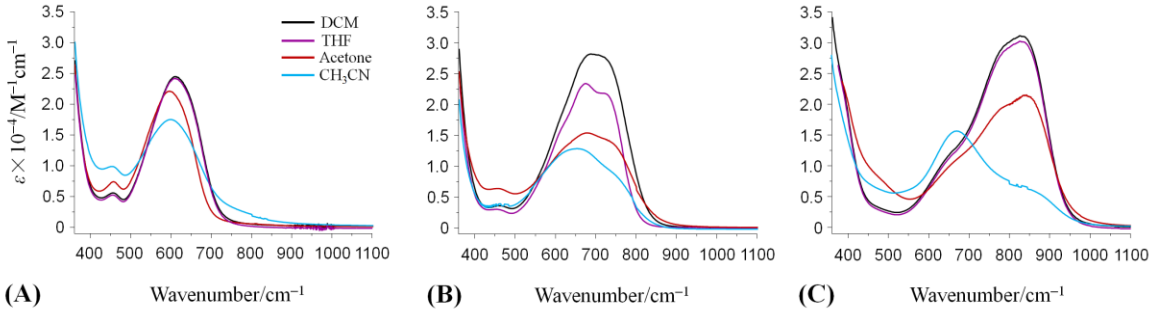


**Figure S3. Electronic spectra of the complexes in dipolar solvents, related to Table 1.** Electronic spectra of the complexes (A) [**thi-(NS)$_2$**], (B) [**thi-OS)$_2$**], and (C) [**thi-(SS)$_2$**] in dipolar THF (purple), acetone (brick red), and acetonitrile (cyan) are compared with dichloromethane (black).

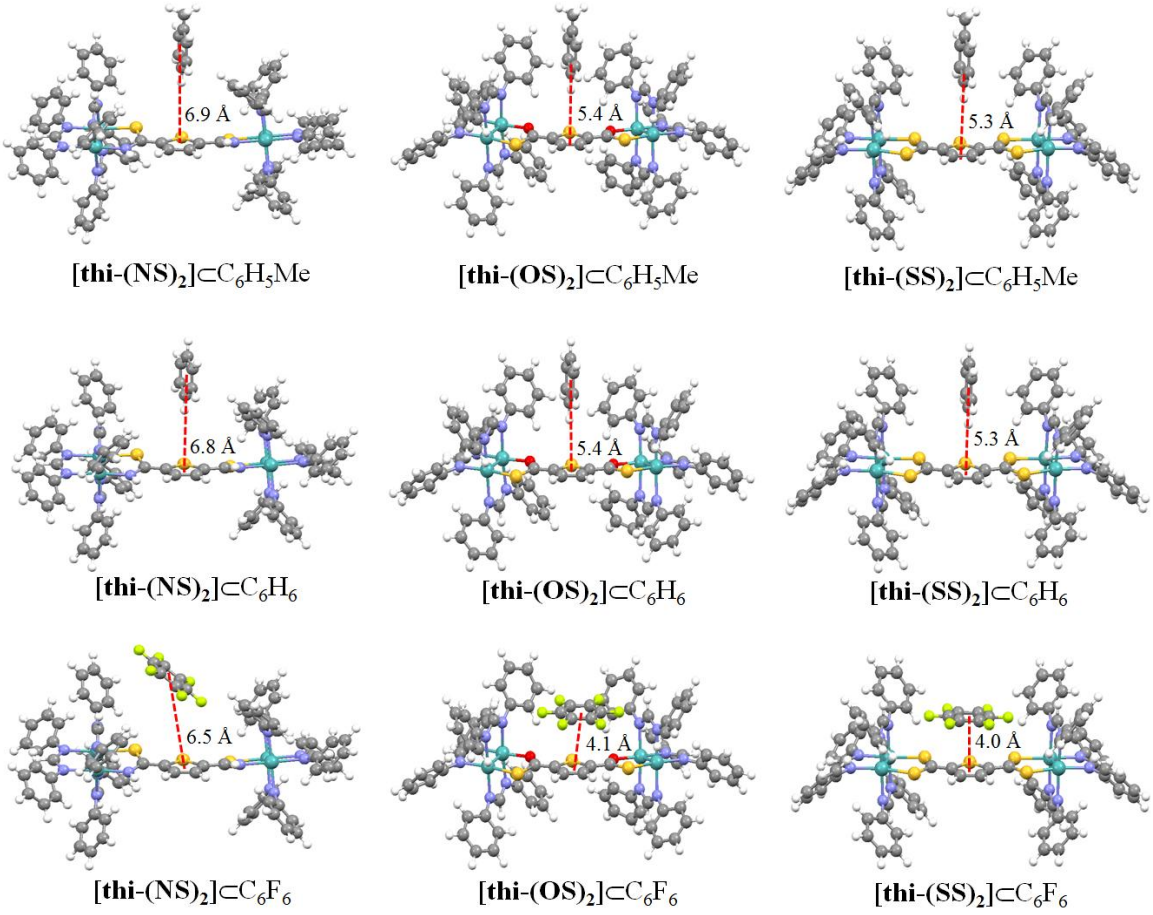


**Figure S4. DFT energy-minimized geometries of the $Mo_2$ models encapsulating aromatic solvent molecule in the cavity of the complexes, related to Figure 4.** Methoxy groups of DAniF ligands are replaced with hydrogen atoms to reduce the computational expense. The centroid distances between the host moiety ($C_4H_2S$) and guest solvent molecule represent the strength of quadrupole interaction.

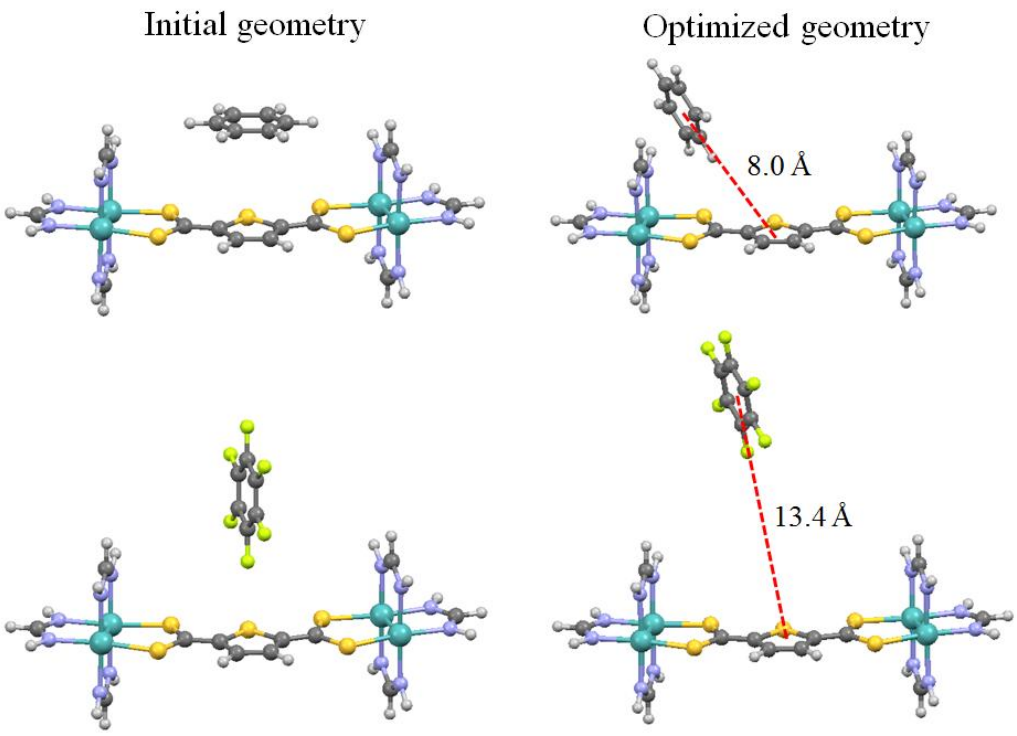


**Figure S5. DFT energy optimization results for [thi-$(SS)_2$]′⊂$C_6H_6$ and [thi-$(SS)_2$]′⊂$C_6F_6$ starting with different host-guest geometries, related to Figure 4.** Optimization reached the configurations without aromatic-aromatic interactions. Here, simplified complex models are used, the same as those for DFT calculations of molecular orbitals (see Figure 4d, Supplemental Figures S6 and S7), because optimization of the complex models with auxiliary ligands DPhF as used in the space-filling models did not reach the convergent results.

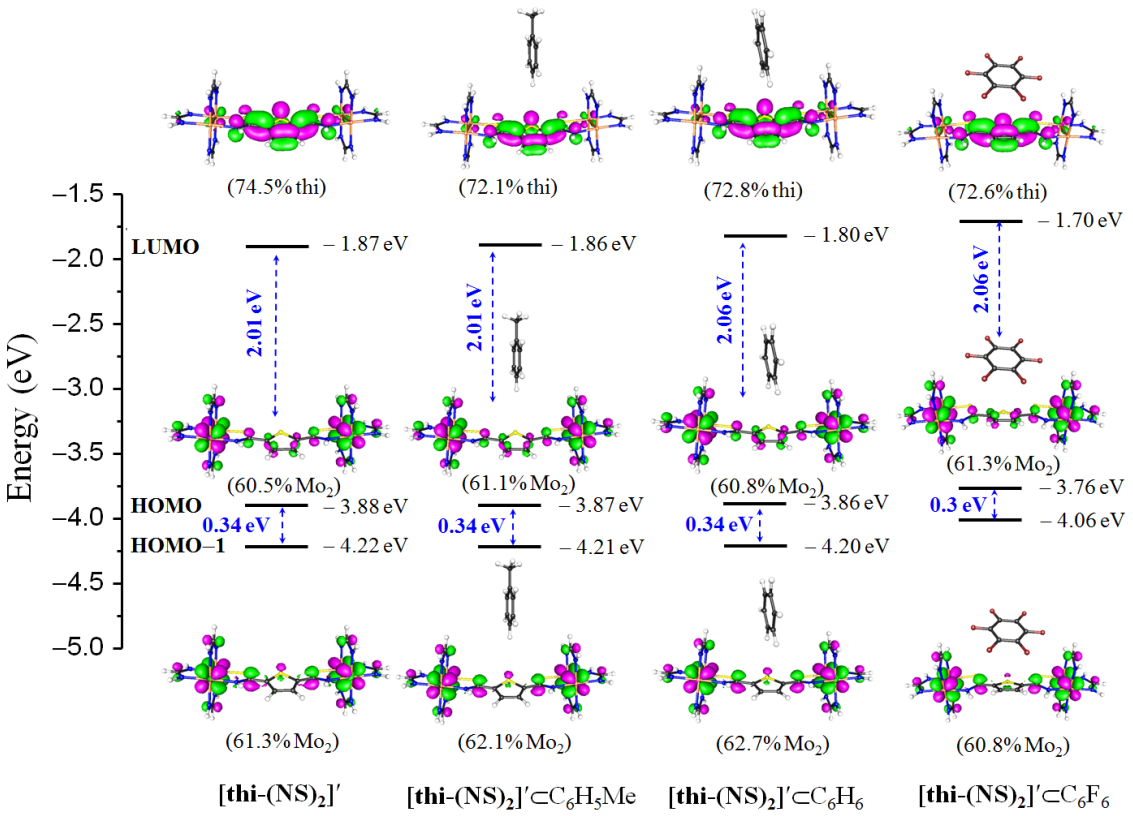


**Figure S6. Frontier molecular orbitals energy levels for the simplified models [thi-$(NS)_2$]′, [thi-$(NS)_2$]′⊂$C_6H_5Me$, [thi-$(NS)_2$]′⊂$C_6H_6$, and [thi-$(NS)_2$]′⊂$C_6F_6$, related to Table 1 and Figure 4.** Frontier molecular orbitals are drawn with isodensity value ±0.02, showing relative orbital energies, the HOMO−LUMO energy gaps and density contributions of metal center ($Mo_2$), bridging ligand (thi) and solvent molecule (SM) to the MOs.

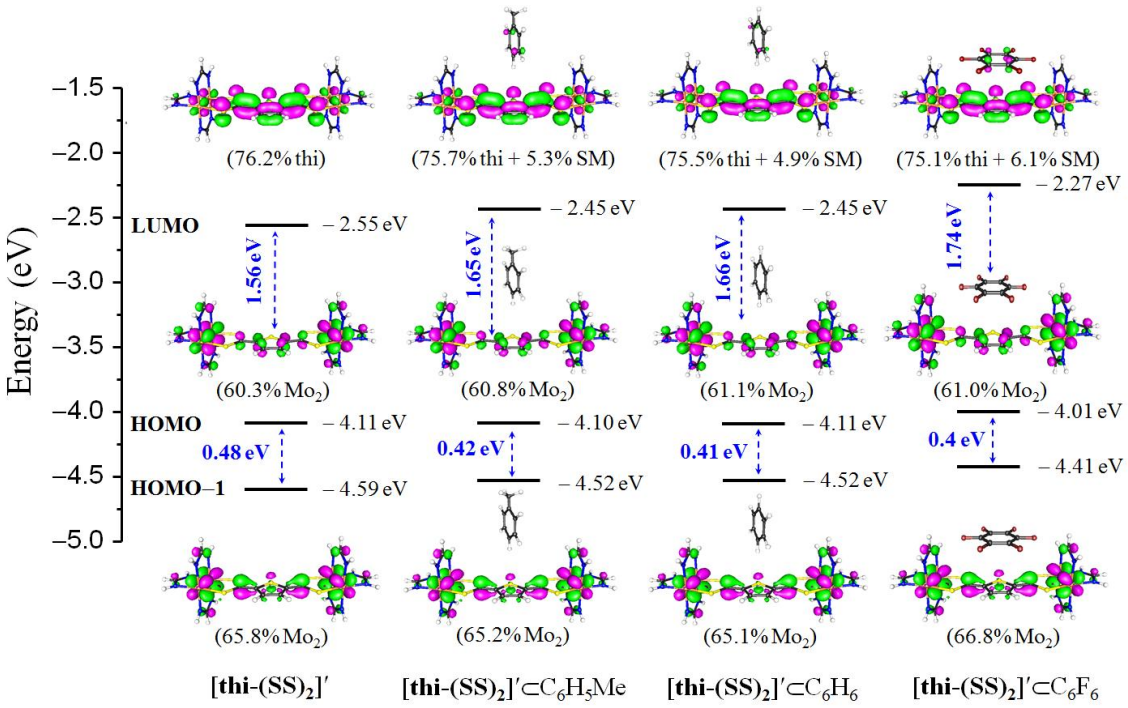


**Figure S7. Frontier molecular orbitals energy levels for the simplified models [thi-$(SS)_2$]′, [thi-$(SS)_2$]′⊂$C_6H_5Me$, [thi-$(SS)_2$]′⊂$C_6H_6$, and [thi-$(SS)_2$]′⊂$C_6F_6$, related to Table 1 and Figure 4.** Frontier molecular orbitals are drawn with isodensity value ±0.02, showing relative orbital energies, the HOMO−LUMO energy gaps and density contributions of metal center ($Mo_2$), bridging ligand (thi) and solvent molecule (SM) to the MOs.

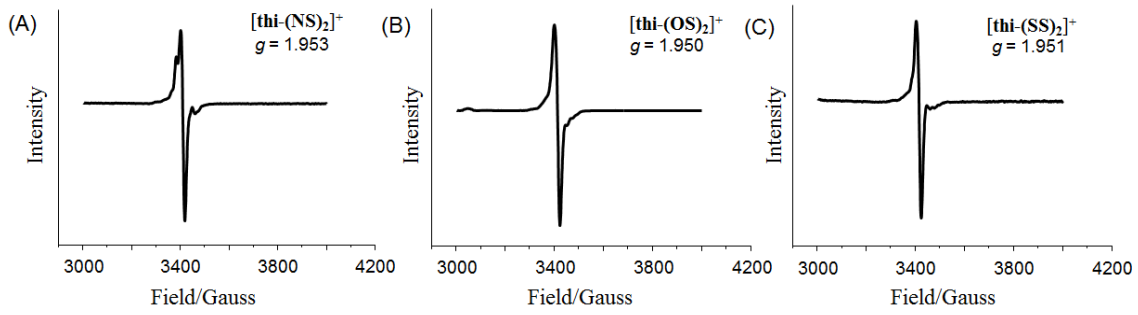


**Figure S8. EPR spectra of the mixed-valence complexes, related to Table 2 and Figure 5.** EPR spectra of (A) [**thi-(NS)$_2$**]$^+$, (B) [**thi-OS)$_2$**]$^+$, and (C) [**thi-(SS)$_2$**]$^+$ were measured *in situ* in toluene solutions at 173 K. For all the complexes, the EPR spectrum shows one peak with some hyperfine structures. The *g* values of 1.950–1.953 are significantly smaller than 2.0023 for an organic radical, indicating that the odd electron resides mainly on a metal-based orbital.

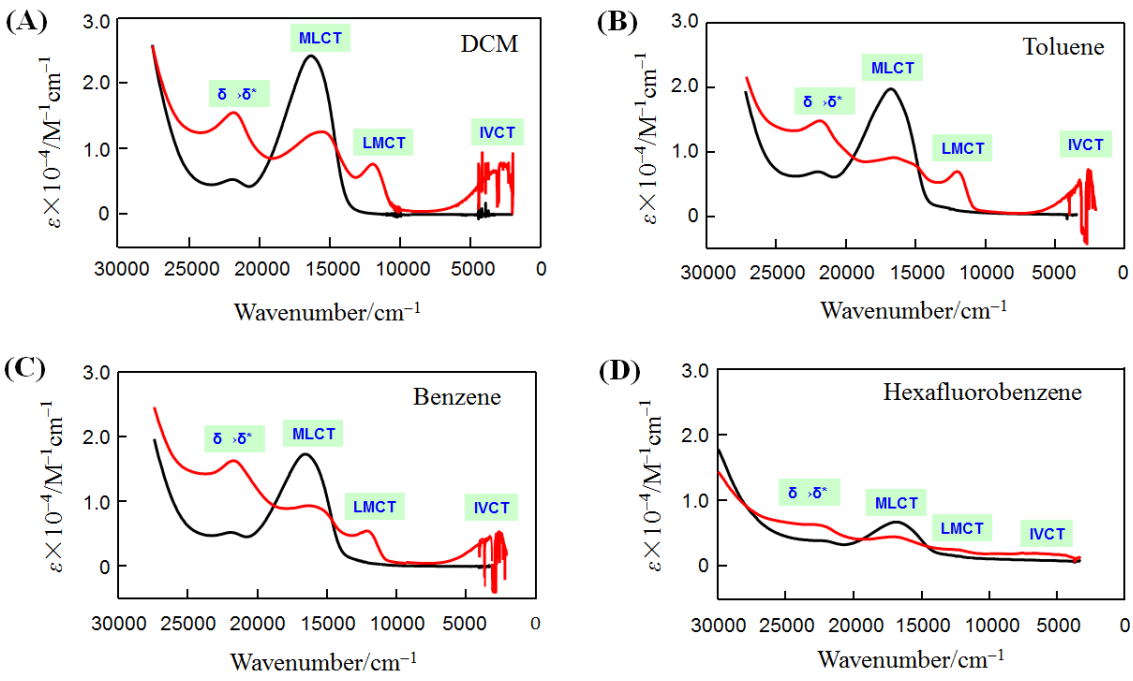


**Figure S9. Comparison of the Vis-near-mid-IR spectra for the mixed-valence complex [thi-(NS)$_2$]$^+$ and its neutral precursor in different solvents, related to Table 1 and Table 2.** Vis-near-mid-IR spectra for the mixed-valence complex [**thi-(NS)$_2$**]$^+$ (red) and its neutral precursor (black) are compared in (A) DCM, (B) Toluene, (C) Benzene, and (D) Hexafluorobenzene solutions.

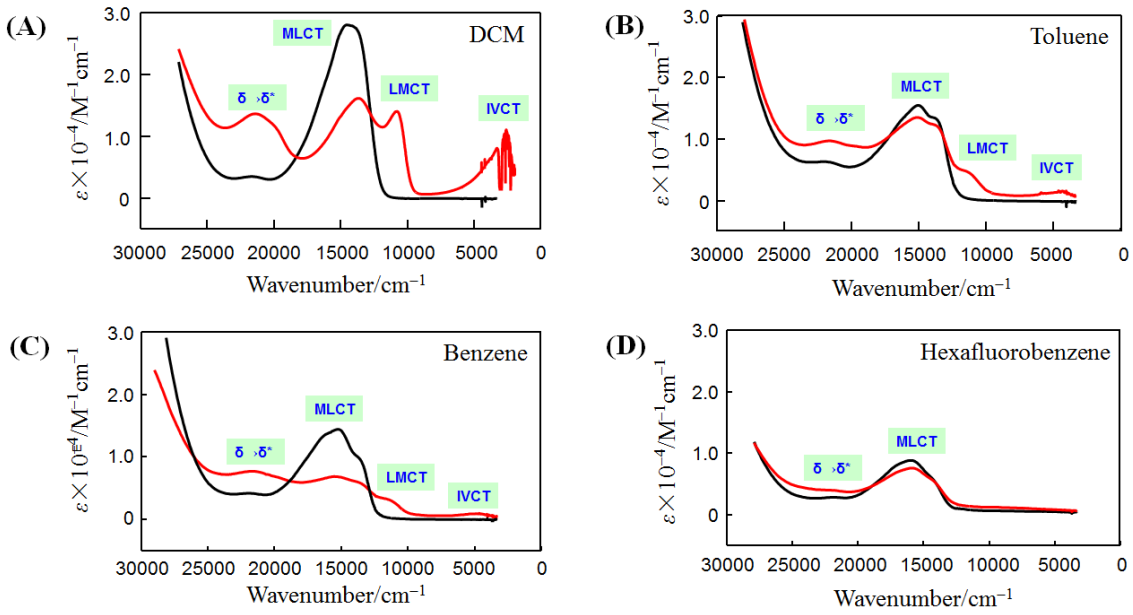


**Figure S10. Comparison of the Vis-near-mid-IR spectra for the mixed-valence complex [thi-(OS)$_2$]$^+$ and its neutral precursor in different solvents, related to Table 1 and Table 2.** Vis-near-mid-IR spectra for the mixed-valence complex [**thi-(OS)$_2$**]$^+$ (red) and its neutral precursor (black) are compared in (A) DCM, (B) Toluene, (C) Benzene, and (D) Hexafluorobenzene solutions.

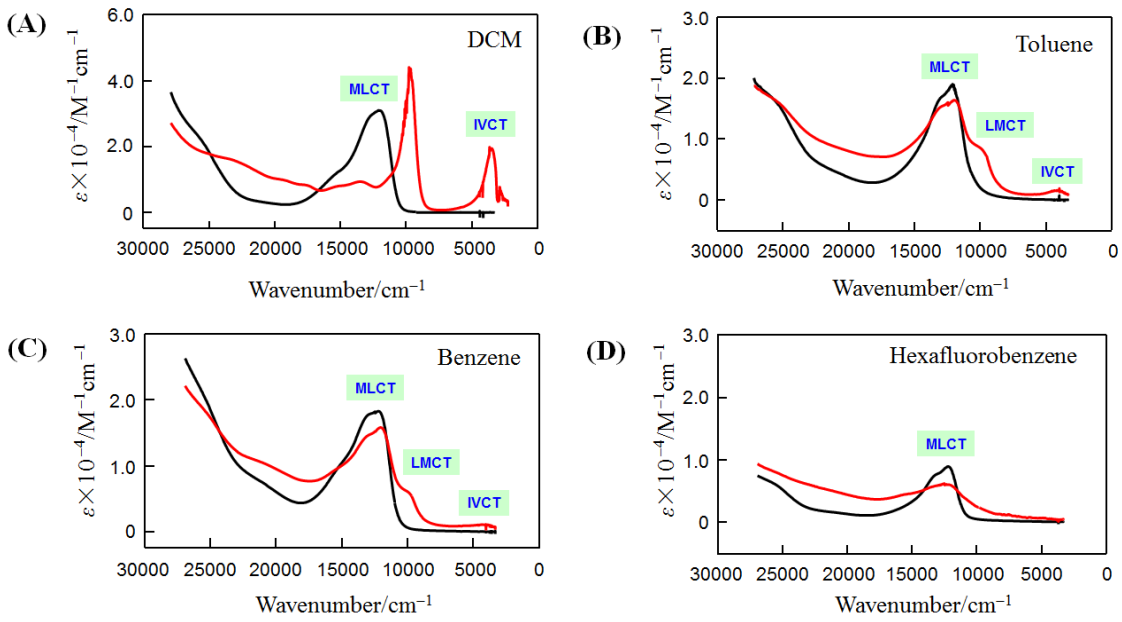


**Figure S11. Comparison of the Vis-near-mid-IR spectra for the mixed-valence complex [thi-(SS)$_2$]$^+$ and its neutral precursor in different solvents, related to Table 1 and Table 2.** Vis-near-mid-IR spectra for the mixed-valence complex [**thi-(SS)$_2$**]$^+$ (red) and its neutral precursor (black) are compared in (A) DCM, (B) Toluene, (C) Benzene, and (D) Hexafluorobenzene solutions.

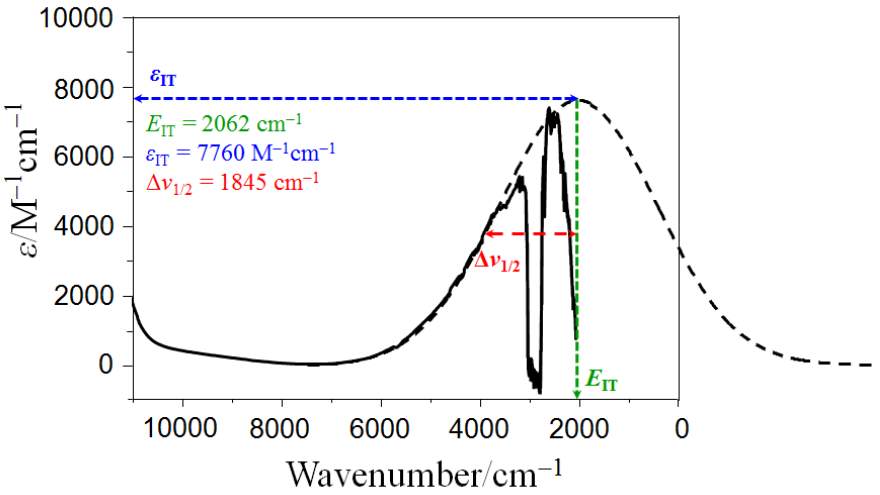


**Figure S12. Extraction of IVCT band parameters for the MV complex [thi-(NS)$_2$]$^+$ in toluene, related to Table 2.** IVCT band parameters ($E_{IT}$, $\mathcal{E}_{IT}$ and $\Delta\nu_{1/2}$) are extracted by Gaussian-shape simulation (black dotted line) of the absorption band.

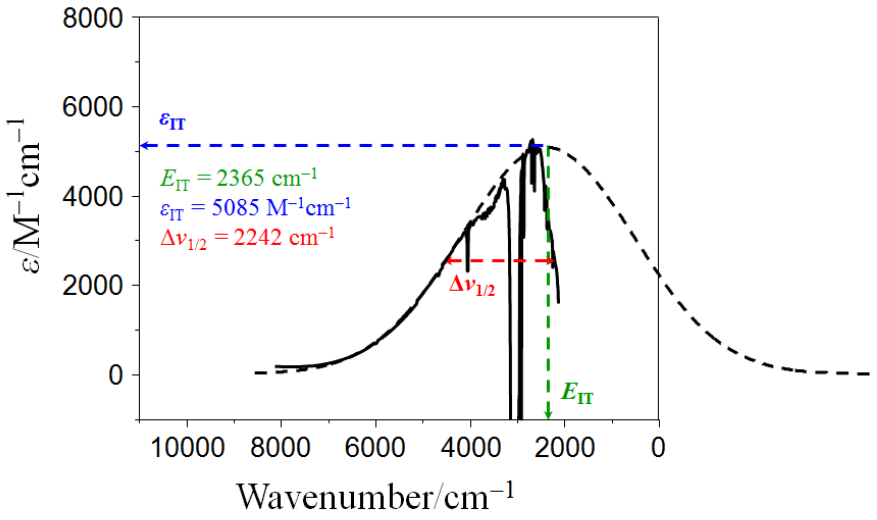


**Figure S13. Extraction of IVCT band parameters for the MV complex [thi-$(NS)_2$]$^+$ in benzene, related to Table 2.** IVCT band parameters ($E_{IT}$, $\varepsilon_{IT}$ and $\Delta\nu_{1/2}$) are extracted by Gaussian-shape simulation (black dotted line) of the absorption band.

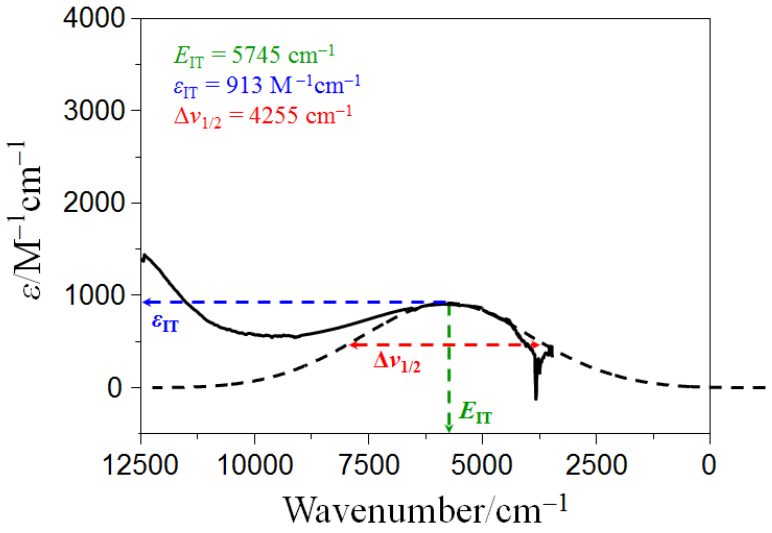


**Figure S14. Extraction of IVCT band parameters for the MV complex [thi-(NS)$_2$]$^+$ in hexafluorobenzene, related to Table 2.** IVCT band parameters ($E_{IT}$, $\varepsilon_{IT}$ and $\Delta\nu_{1/2}$) are extracted by Gaussian-shape simulation (black dotted line) of the absorption band.

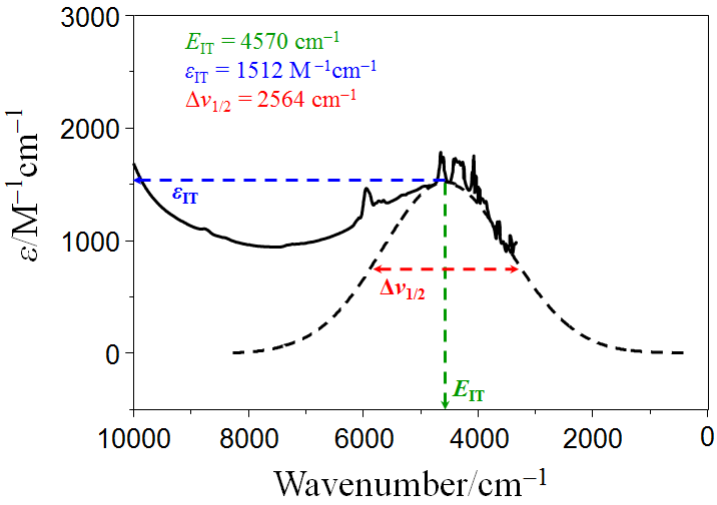


**Figure S15. Extraction of IVCT band parameters for the MV complex [thi-(OS)$_2$]$^+$ in toluene, related to Table 2.** IVCT band parameters ($E_{IT}$, $\mathcal{E}_{IT}$ and $\Delta\nu_{1/2}$) are extracted by Gaussian-shape simulation (black dotted line) of the absorption band.

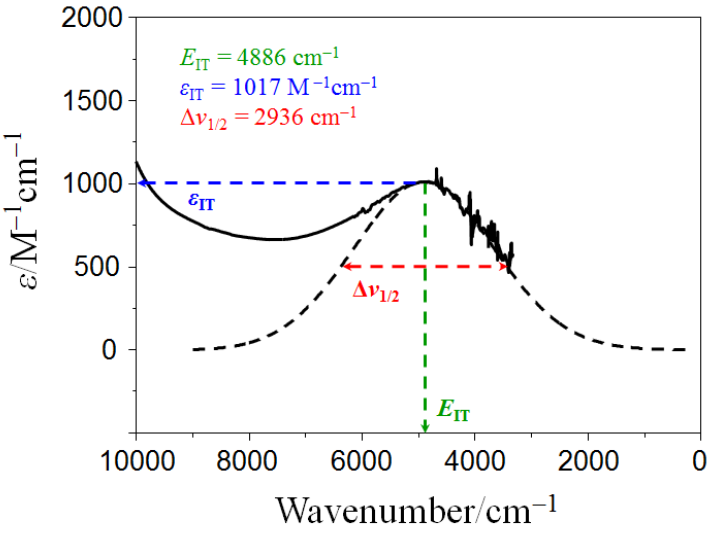


**Figure S16. Extraction of IVCT band parameters for the MV complex [thi-(OS)$_2$]$^+$ in benzene, related to Table 2.** IVCT band parameters ($E_{IT}$, $\varepsilon_{IT}$ and $\Delta\nu_{1/2}$) are extracted by Gaussian-shape simulation (black dotted line) of the absorption band.

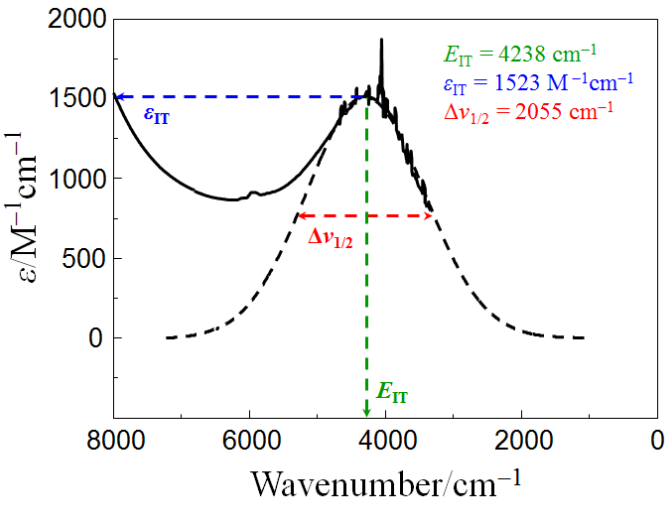


**Figure S17. Extraction of IVCT band parameters for the MV complex [thi-(SS)$_2$]$^+$ in toluene, related to Table 2.** IVCT band parameters ($E_{IT}$, $\mathcal{E}_{IT}$ and $\Delta\nu_{1/2}$) are extracted by Gaussian-shape simulation (black dotted line) of the absorption band.

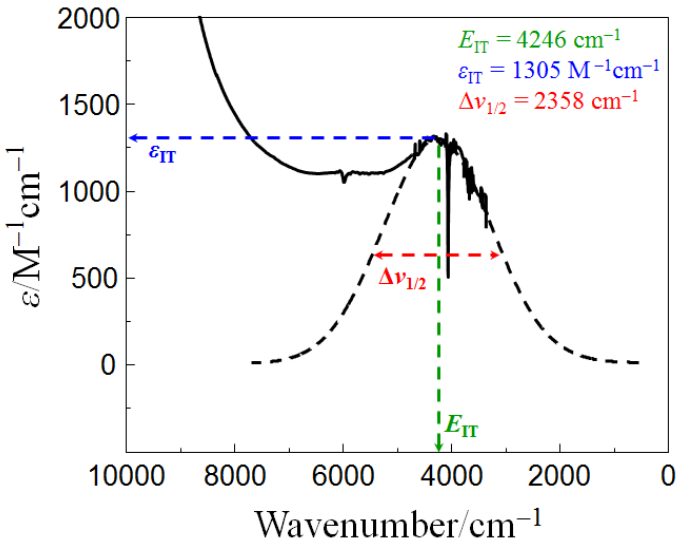


**Figure S18. Extraction of IVCT band parameters for the MV complex [thi-(SS)$_2$]$^+$ in benzene, related to Table 2.** IVCT band parameters ($E_{IT}$, $\varepsilon_{IT}$ and $\Delta\nu_{1/2}$) are extracted by Gaussian-shape simulation (black dotted line) of the absorption band.

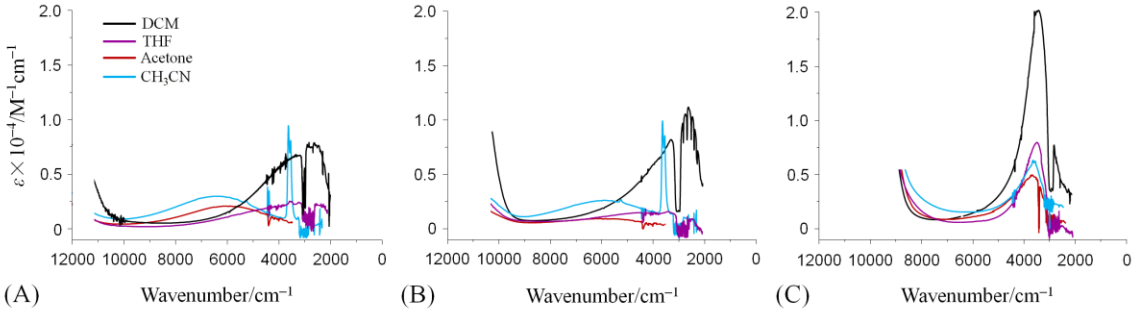


**Figure S19. IVCT absorptions of the MV complexes in dipolar solvents, related to Table 2.** IVCT absorption bands in the near- to mid-IR region of the MV complexes (A) [**thi-(NS)$_2$**]$^+$, (B) [**thi-(OS)$_2$**]$^+$, and (C) [**thi-(SS)$_2$**]$^+$ in dipolar solvents THF (purple), acetone (brick red), and acetonitrile (cyan) are compared with dichloromethane (black).

## Supplemental Table

**Table S1. Crystallographic parameters for [thi-$(NS)_2$], [thi-$(OS)_2$] and [thi-$(SS)_2$], related to Figure 3.**

| | [**thi-$(NS)_2$**] | [**thi-$(OS)_2$**] | [**thi-$(SS)_2$**] |
|---|---|---|---|
| Empirical formula | $C_{96}H_{94}Mo_4N_{14}O_{12}S_3$ | $C_{96}H_{92}Mo_4N_{12}O_{14}S_3$ | $C_{96}H_{92}Mo_4N_{12}O_{12}S_5$ |
| fw | 2115.80 | 2117.75 | 2149.87 |
| space group | $P2_1/c$ | $P\bar{1}$ | $P\bar{1}$ |
| $a$(Å) | 14.4340(4) | 18.5703(4) | 11.5208(6) |
| $b$(Å) | 18.2754(6) | 22.5537(5) | 13.9285(7) |
| $c$(Å) | 19.6516(7) | 29.0785(6) | 18.7648(8) |
| $\alpha$ (deg) | 90.0 | 88.6437(18) | 104.269(4) |
| $\beta$ (deg) | 94.936(3) | 75.4352(18) | 101.332(4) |
| $\gamma$ (deg) | 90.0 | 73.8157(19) | 100.794(4) |
| $V$ (Å$^3$) | 5164.6(3) | 11306.3(4) | 2771.9(2) |
| $Z$ | 2 | 4 | 1 |
| $T$(K) | 238 | 173 | 173 |
| $d_{calcd}$ (g/cm$^3$) | 1.361 | 1.244 | 1.288 |
| $\mu$ (mm$^{-1}$) | 4.960 | 4.540 | 4.966 |
| GOF ($F^2$) | 1.055 | 1.039 | 1.055 |
| $R_1$[a] | 0.0567 | 0.1011 | 0.0564 |
| $wR_2$[b] | 0.1700 | 0.3109 | 0.1537 |

[a] $R_1=\sum||F_o|-|F_c||/\sum|F_o|$. [b] $wR_2=[\sum[w(F_o^2-F_c^2)^2]/\sum[w(F_o^2)^2]]^{1/2}$

**Table S2. Selected bond distances (Å) and tosion angles (°) in [thi-$(NS)_2$], [thi-$(OS)_2$] and [thi-$(SS)_2$], related to Figure 3.**

| | [**thi-$(NS)_2$**] | [**thi-$(OS)_2$**] | [**thi-$(SS)_2$**] |
|---|---|---|---|
| Mo(1)–Mo(2) | 2.1024(7) | 2.1004(11) | 2.1003(7) |
| Mo(3)–Mo(4) | - | 2.1050(13) | - |
| Mo(2)–N(1)/ Mo(2)–O(1)/ Mo(1)–S(4) | 2.15(3) | 2.103(7) | 2.551(4) |
| Mo(1)–S(1)/ Mo(2)–S(1)/ Mo(2)–S(3) | 2.480(9) | 2.486(3) | 2.551(8) |
| C(1)–N(1)/C(1)–O(1)/C(1)–S(2) | 1.317(17) | 1.263(14) | 1.62(3) |
| C(1)–S(1) | 1.666(15) | 1.719(10) | 1.699(14) |
| C(1)···C(6) | 5.325 | 5.271 | 5.326 |
| $Mo_2$···$Mo_2$ | 11.251 | 10.702 | 11.556 |
| Torsion Angle | 27.35 | 3.42 | 7.76 |

**Table S3. MLCT band parameters for [thi-$(NS)_2$], [thi-$(OS)_2$] and [thi-$(SS)_2$] in dipolar solvents THF, acetone and $CH_3CN$, compared to $CH_2Cl_2$, related to Table 1.**

| | [**thi-$(NS)_2$**] | | [**thi-$(OS)_2$**] | | [**thi-$(SS)_2$**] | |
|---|---|---|---|---|---|---|
| | $E_{ML}$ (nm) | $\varepsilon_{ML}$ ($M^{-1}cm^{-1}$) | $E_{ML}$ (nm) | $\varepsilon_{ML}$ ($M^{-1}cm^{-1}$) | $E_{ML}$ (nm) | $\varepsilon_{ML}$ ($M^{-1}cm^{-1}$) |
| $CH_2Cl_2$ | 611 | 24455 | 680 | 28175 | 790 | 29670 |
| THF | 610 | 24320 | 675 | 23320 | 789 | 29595 |
| Acetone | 593 | 22035 | 672 | 15315 | 785 | 19525 |
| $CH_3CN$ | 595 | 17465 | 650 | 12820 | 668 | 15595 |

**Table S4. IVCT band parameters for [thi-$(NS)_2$], [thi-$(OS)_2$] and [thi-$(SS)_2$] in dipolar solvents THF, acetone and $CH_3CN$, compared to $CH_2Cl_2$, related to Table 2.**

| | [**thi-$(NS)_2$**] | | | [**thi-$(OS)_2$**] | | | [**thi-$(SS)_2$**] | | |
|---|---|---|---|---|---|---|---|---|---|
| | $E_{IT}$ ($cm^{-1}$) | $\varepsilon_{IT}$ ($M^{-1}cm^{-1}$) | $\Delta\nu_{1/2}$ (exp) ($cm^{-1}$) | $E_{IT}$ ($cm^{-1}$) | $\varepsilon_{IT}$ ($M^{-1}cm^{-1}$) | $\Delta\nu_{1/2}$ (exp) ($cm^{-1}$) | $E_{IT}$ ($cm^{-1}$) | $\varepsilon_{IT}$ ($M^{-1}cm^{-1}$) | $\Delta\nu_{1/2}$ (exp) ($cm^{-1}$) |
| $CH_2Cl_2$ | 2630 | 7933 | 2480 | 2254 | 11398 | 2009 | 3290 | 20261 | 1266 |
| THF | 3188 | 2280 | 3733 | 4355 | 1460 | 4387 | 3310 | 7965 | 965 |
| Acetone | 5970 | 2110 | 3695 | 5885 | 940 | 4130 | 3390 | 5005 | 1320 |
| $CH_3CN$ | 6396 | 2985 | 3960 | 5910 | 2600 | 4300 | 3317 | 6150 | 1197 |

## Transparent Methods

All manipulations were performed in a nitrogen-filled glovebox or by using standard Schlenk-line techniques. All solvents were freshly distilled over appropriate drying agents and collected for further use under a nitrogen atmosphere. HDAniF (Lin et al., 1996), $Mo_2(DAniF)_3(O_2CCH_3)$ (Cotton et al., 2003), and $Mo_2$ dimers [**thi-(NS)$_2$**], [**thi-(OS)$_2$**], and [**thi-(SS)$_2$**] (Wu et al., 2017) were synthesized according to published methods.

**Electrochemical studies.** Electrochemical measurements on the neutral compounds were carried out in 0.1M tetrahexylammonium hexafluorophosphate / toluene and dichloromethane solutions. The CVs and differential pulse voltammograms were obtained using a CH Instruments model CHI660D electrochemical analyzer with Pt working and auxiliary electrodes, and Ag/AgCl reference electrode with a scan rate of 100 mV/s. Under these conditions, the redox potential for ferrocene, $E_{1/2}(Fc^{+/0})$, is 0.52 V. The measured potentials for the complexes are referenced to $E_{1/2}(Fc^{+/0})$. The redox potential separation ($\Delta E_{1/2}$) value in toluene are estimated from the working curve based on the Richardson–Taube method (Richardson and Taube, 1981).

**Spectroscopic measurements.** UV-vis-NIR spectra were measured in $CH_2Cl_2$, toluene, benzene, and hexafluorobenzene solutions using IR quartz cells with a light path length of 2 mm on a Shimadzu UV-3600 UV-vis-NIR spectrophotometer. EPR spectra of the mixed-valence complexes were measured using a Bruker A300-10-12 electron paramagnetic resonance spectrometer.

**X-ray structure determination.** Single-crystal data for [**thi-(NS)$_2$**], [**thi-(OS)$_2$**], and [**thi-(SS)$_2$**] were collected on a Rigaku XtaLAB Pro diffractometer with Cu-Kα radiation ($\lambda$ = 1.54178 Å). Compound [**thi-(NS)$_2$**] crystallized in a monoclinic space group $P2_1/c$ with Z = 2, while [**thi-(OS)$_2$**], and [**thi-(SS)$_2$**] in a triclinic space group $P\bar{1}$ with Z = 1. The empirical absorption corrections were applied using spherical harmonics, implemented in the SCALE3 ABSPACK scaling algorithm. The structures were solved using direct methods, which yielded the positions of all non-hydrogen atoms. Hydrogen atoms were

placed in calculated positions in the final structure refinement. Structure determination and refinement were carried out using the SHELXS-2014 and SHELXL-2014 programs, respectively (Sheldrick, 2000). The unit cell volume included a large region of disordered solvent which could not be modelled as discrete atomic sites. The treatment for the guest molecules in the cavities of all crystals involves the use of the SQUEEZE program of PLATON (Spek, 2003).

**Computational details.** The ORCA 2.9.1 software package (Neese, 2012) was used for all DFT computations assuming an $S = 0$ spin state. The geometry of the model complexes incorporating solvent molecule was optimized in the gas phase, employing the Becke−Perdew (BP86) functional (Perdew, 1986; Becke, 1988) and RI/J approximation (Neese, 2003). Geometry optimizations for the complexes were converged with the def2-SV(P) basis set (Schäfer et al., 1992) and def2-SVP/J auxiliary basis set (Eichkorn et al., 1995; Eichkorn et al., 1997) for C and H atoms, def2-TZVP(−f) basis set (Weigend and Ahlrichs, 2005) and def2-TZVP/J auxiliary basis set (Neese, 2012) for S, N, and O atoms. For Mo atoms def2-TZVPP basis set (Perdew, 1986; Becke, 1988) and def2-TZVPP/J auxiliary basis set (Neese, 2012) were used together with scalar relativistic effects by the zeroth-order regular approximation (ZORA) (Pantazis et al., 2008). Tight optimization and tight self-consistent field convergence were employed along with a dense integration grid (ORCA Grid 5) for all geometry optimization calculations. Single-point energy (SPE) calculations on optimized geometries were performed using the B3LYP functional (Becke, 1993; Lee et al., 1988) and the COSMO methodology (Klamt and Schüürmann, 1993). Isosurface plots of molecular orbitals were generated using the gOpenMol 3.00 program (Laaksonen, 1992; Bergman et al., 1997) with isodensity values ± 0.02.

Amsterdam Density Functional (ADF) suite (te Velde et al., 2001; Fonseca Guerra et al., 1998) was used to generate the electrostatic potential map from the SPE calculation on the simplified models encapsulating solvent molecule, employing the BP86 functional and an all-electron triple-ζ basis set with a polarization function on all atoms (TZP) together with ZORA approximation. The electrostatic potential mapped on the electron density with an isodensity value of 0.04. The color range were adjusted to the same scale, thus a direct comparison between electrostatic potential maps is viable.

## Supplemental References


Lin, C., Protasiewicz, J. D., Smith, E. T., and Ren, T. (1996). Linear Free Energy Relationships in Dinuclear Compounds. 2. Inductive Redox Tuning via Remote Substituents in Quadruply Bonded Dimolybdenum Compounds. Inorg. Chem. *35*, 6422−6428.

Cotton, F. A., Liu, C. Y., Murillo, C. A., Villagrán, D., and Wang, X. (2003). Modifying Electronic Communication in Dimolybdenum Units by Linkage Isomers of Bridged Oxamidate Dianions. J. Am. Chem. Soc. *125*, 13564−13575.

Wu, Y. Y., Meng, M., Wang, G. Y., Feng, P., and Liu, C. Y. (2017). Optically probing the localized to delocalized transition in $Mo_2$–$Mo_2$ mixed-valence systems. Chem. Commun. *53*, 3030−3033.

Richardson, D. E., and Taube, H. (1981). Determination of $E_2^0$ - $E_1^0$ in multistep charge transfer by stationary-electrode pulse and cyclic voltammetry: application to binuclear ruthenium ammines. Inorg. Chem. *20*, 1278 −1285.

CrysAlis, C. and CrysAlis RED, version 1.171.31.7, (Oxford Diffraction Ltd, Abingdon, U. K., 2006).

Sheldrick, G. M. (2000). SHELXTL, version 6.12, (Bruker Analytical X-ray Systems, Inc., Madison, WI).

Spek, A. L. (2003). Single-crystal structure validation with the program PLATON. J. Appl. Crystallogr. *36*, 7−13.

Neese, F. (2012). The ORCA program system. WIREs Comput. Mol. Sci. *2*, 73−78.

Perdew, J. P. (1986). Density-functional approximation for the correlation energy of the inhomogeneous electron gas. Phys. Rev. B: Condens. Matter Mater. Phys. *33*, 8822−8824.

Becke, A. D. (1988). Density-functional exchange-energy approximation with correct asymptotic behavior. Phys. Rev. A: At., Mol., Opt. Phys. *38*, 3098−3100.

Neese, F. (2003). An improvement of the resolution of the identity approximation for the formation of the Coulomb matrix. J. Comput. Chem. *24*, 1740−1747.

Schäfer, A., Horn, H., and Ahlrichs, R. (1992). Fully optimized contracted Gaussian basis sets for atoms Li to Kr. J. Chem. Phys. *97*, 2571−2577.

Eichkorn, K., Treutler, O., Öhm, H., Häser, M., and Ahlrichs, R. (1995). Auxiliary basis sets to approximate Coulomb potentials. Chem. Phys. Lett. *240*, 283−290.

Eichkorn, K., Weigend, F., Treutler, O., and Ahlrichs, R. (1997). Auxiliary basis sets for main row atoms and transition metals and their use to approximate Coulomb potentials. Theor. Chem. Acc. *97*, 119−124.

Weigend, F., and Ahlrichs, R. (2005). Balanced basis sets of split valence, triple zeta valence and quadruple zeta valence quality for H to Rn: Design and assessment of accuracy. Phys. Chem. Chem. Phys. *7*, 3297−3305.

Pantazis, D. A., Chen, X.-Y., Landis, C. R., and Neese, F. (2008). All Electron Scalar Relativistic Basis Sets for Third-Row Transition Metal Atoms. J. Chem. Theory Comput. *4*, 908−919.

Becke, A. D. (1993). A new mixing of Hartree-Fock and local density-functional theories. J. Chem. Phys. *98*, 1372−1377.

Becke, A. D. (1993). Density-functional thermochemistry. III. The role of exact exchange. J. Chem. Phys. *98*, 5648−5652.

Lee, C., Yang, W., and Parr, R. G. (1988). Development of the Colle-Salvetti correlation-energy formula into a functional of the electron density. Phys. Rev. B: Condens. Matter Mater. Phys. *37*, 785−789.

Klamt, A., and Schüürmann, G. (1993). COSMO: A new approach to dielectric screening in solvents with explicit expressions for the screening energy and its gradient. J. Chem. Soc., Perkin Trans. 2 *5*, 799−805.

Laaksonen, L. (1992). A graphics program for the analysis and display of molecular dynamics trajectories. J. Mol. Graphics *10*, 33−34.

Bergman, D. L., Laaksonen, L., and Laaksonen, A. (1997). Visualization of solvation structures in liquid mixtures. J. Mol. Graphics Modell. *15*, 301−306.

te Velde et al. (2001). Chemistry with ADF. J. Comput. Chem. *22*, 931−967.

Fonseca Guerra, C., Snijders, J. G., te Velde, G., and Baerends, E. J. (1998). Theor. Chem. Acc. *99*, 391−403.